UNIVERSITY OF LEEDS

This is a repository copy of *Flow cell apparatus for quantitative evaluation of carbon steel corrosion during transitions in fluid composition: Application to transition from inhibited hydrochloric acid to sodium chloride brine*.

White Rose Research Online URL for this paper:
http://eprints.whiterose.ac.uk/130232/

Version: Accepted Version

Article:
Barker, R orcid.org/0000-0002-5106-6929, Pickles, B, Kapur, N orcid.org/0000-0003-1041-8390 et al. (3 more authors) (2018) Flow cell apparatus for quantitative evaluation of carbon steel corrosion during transitions in fluid composition: Application to transition from inhibited hydrochloric acid to sodium chloride brine. Corrosion Science, 138. pp. 116-129. ISSN 0010-938X

https://doi.org/10.1016/j.corsci.2018.04.012

© 2018 Elsevier Ltd. This manuscript version is made available under the CC-BY-NC-ND 4.0 license http://creativecommons.org/licenses/by-nc-nd/4.0/

Reuse
This article is distributed under the terms of the Creative Commons Attribution-NonCommercial-NoDerivs (CC BY-NC-ND) licence. This licence only allows you to download this work and share it with others as long as you credit the authors, but you can't change the article in any way or use it commercially. More information and the full terms of the licence here: https://creativecommons.org/licenses/

Takedown
If you consider content in White Rose Research Online to be in breach of UK law, please notify us by emailing eprints@whiterose.ac.uk including the URL of the record and the reason for the withdrawal request.

White Rose university consortium
Universities of Leeds, Sheffield & York

eprints@whiterose.ac.uk
https://eprints.whiterose.ac.uk/

Flow cell apparatus for quantitative evaluation of carbon steel corrosion during transitions in fluid composition: Application to transition from inhibited hydrochloric acid to sodium chloride brine

Richard Barker[a*], Benjamin Pickles[a], Nik Kapur[a], Trevor Hughes[b], Evgeny Barmatov[b] and Anne Neville[a]

[a]Institute of Functional Surfaces, School of Mechanical Engineering, University of Leeds, Leeds, LS2 9JT, UK
[b]Schlumberger Cambridge Research, High Cross, Madingley Road, Cambridge, CB3 OEL, UK
*Corresponding Author R.J.Barker@leeds.ac.uk

Abstract

This paper introduces a new flow cell technique that offers the advantage of real-time corrosion rate behaviour acquired as transitions in fluid chemistry occur using in situ electrochemistry. The present study quantifies the corrosion behaviour of a metal surface initially exposed to inhibited acid and subsequently exposed to a model formation brine. The design, optimisation and validation of the flow cell set-up is discussed. Results from initial tests show that inhibition efficiency and steel corrosion rate change significantly during the dilution process as the inhibitor film experiences concomitant changes in the “external” concentrations of acid and propargyl alcohol inhibitor.

Keywords: Acid solutions (A), Carbon steel (A), Electrochemical calculation (B), Weight loss (B), Acid corrosion inhibitor (C)

1. Introduction

Three types of acid treatments exist as a means of increasing hydrocarbon production from oil and gas reservoirs: acidic flushing of wells (in order to remove acid-soluble well sediments), acid fracturing (whereby acid is injected into the formation above the fracture pressure), and matrix acidizing. The method of matrix acidizing [1-3] is one of the most widely used techniques to enhance the rate of production from hydrocarbon reservoirs. The process involves injecting acid into the near-wellbore rock at a flow rate below that required to exceed the fracturing pressure. The acid is designed to partially dissolve the reservoir rock, e.g. forming “wormholes” in carbonate rocks, or to dissolve permeability-damaging materials introduced during drilling, completion, or production operations, e.g. as in sandstone acidizing treatments. The acid reacts with rock minerals and damaging materials to create soluble products that can be easily removed when production is resumed. It is essential the acid is sufficiently “inhibited” to minimise corrosion of metals in the wellbore. Acid Corrosion Inhibitor (ACI) products are complex mixtures of various molecules designed to minimise the rate of corrosion of oilfield steels and alloys

Schlumberger-Private

exposed to typical matrix acids under high-temperature and high-pressure conditions.

Typical matrix acidizing fluids contain hydrochloric acid, hydrochloric acid/hydrofluoric acid mixtures, acetic acid, and formic acid [1-3]. New fluids were developed to extend matrix acidizing to higher temperatures. For example, acid-internal emulsions retard reaction rates in carbonate reservoirs and mild, slightly acidic chelating agents are used in carbonates and sandstones [4]. In sandstone acidizing, the combination of hydrochloric acid and hydrofluoric acid is used to ensure dissolution of silicate minerals, and complex multistage treatments are used to minimise the potential for detrimental effects due to secondary precipitation [1-3, 5-7].

Matrix acidizing fluids are either pumped directly into the well or delivered into target zone(s) via coiled tubing. Regardless of the injection method, all such fluids must contain the appropriate ACI chemistry and dosage to minimise the corrosion of all contacted metal and alloy surfaces. Typical ACI chemistries were recently reviewed by Finšgar and Jackson [8]. An important class of ACIs used in high-temperature acidizing are “polymerisable inhibitors” such as the acetylenic alcohols (e.g. propargyl alcohol (PA), or 4-ethyl-1-octyn-3-ol) [8, 9]. These molecules readily adsorb on metal surfaces and undergo acid and metal surface initiated polymerisation to form a protective polymeric inhibitor film [10-15].

One particular concern for operators is when the production of oil is restarted after a matrix acidizing treatment. There can be a period during which residual or unspent acid flows into the well followed by formation fluids. Such a process is termed “acid flowback” and it is important to minimise its effect on the integrity of wellbore and surface equipment. Quantifying the effect of this process is challenging because the unspent acid containing inhibitor is progressively diluted by formation fluids.

The extent to which the injected acid is fully spent or neutralised prior to resuming production depends on many factors including (i) the composition and reactivity of the acidizing fluid; (ii) the composition, heterogeneity, and reactivity of the treated rock; and (iii) treatment details such as the volume and composition of pre-flush and post-flush fluids, shut-in time, and flowback procedures. Therefore, in certain situations, the near-wellbore region of the treated zone(s) contains residual unspent acid that flows back into the wellbore and to the surface when production is resumed. In such cases, the quantity of unspent acid can be quantified by pH and chemical monitoring of the flowback fluids. Some publications indicate acid flowback fluids can have a pH in the region 0–3 [16-18]. Other field cases show acid flowback fluids are fully neutralised [19] or can be neutralised by special flowback procedures [20]. A recent publication [21] reports on the corrosivity of partially spent acids in contact with a range of different carbon steels, both low and high alloys; it is emphasised that partially spent hydrochloric/hydrofluoric acids are highly corrosive for 13Cr, duplex stainless steels and titanium alloys.

Schlumberger-Private

This paper introduces a new flow cell technique that can quantify the progressive corrosion behaviour of a metal surface initially exposed to inhibited acid (simulating unspent acid) and subsequently exposed to increasing dilutions by an uninhibited brine solution (simulating the formation brine). In principle, the technique can be applied to any given acid flowback scenario wherein a metal surface is exposed to a sequence of acid flowback fluids including the post-flush, the partially spent main acid stage, the pre-flush, and the formation brine.

The application of customised flow cells to understand the corrosion behaviour of metals in specific aqueous environments relating to industrial processes is not a new concept. In 1965, Barcarella and Sutton [22] utilised a once-through flow cell to study the rate of film growth on zirconium and Zircaloy-2 in oxygenated sulphuric acid using electrochemical methods. The once-through nature prevented solution contamination and employed a flow rate of 1 ml min^{-1} through a cell of 50 ml capacity. More recent developments of flow cells include the work of Stupnisek-Lisac et al. [23] who evaluated the inhibition of copper in HCl environments. Their recirculating system consisted of a three-electrode setup within a 500 ml volume cell. The apparatus was able to circulate 0.5 mol L^{-1} HCl at a flow rate of 400 to 4000 ml min^{-1} to determine the effect of an imidazole derivative on corrosion inhibition.

Flow cells have also seen application in the context of microbial pitting corrosion. Here Duncan et al. [24] developed a 375 ml capacity flow cell with a flow rate of 0.65 ml min^{-1}. Although the system was once-through, it was not instrumented for electrochemical measurements. In relation to systems which bear a relation to the flow regimes encountered in industrial systems, Postlethwaite and Brierley [25] developed a flow cell integrated with electrodes for electrochemical measurement, capable of operating in the turbulent flow regime in alkaline environments up to 300^{o}C and 8.5 MPa within a recirculating flow loop. In a similar arrangement, Wharton and Wood [26] developed an electrochemical flow cell which was positioned within a recirculating system capable of generating flow with fully developed hydrodynamic and mass transfer boundary layers, before the electrolyte reached the test specimens. The system was able to generate flow velocities between 0.04 and 2.7 m s^{-1} (corresponding to Reynolds numbers in the range 1000-75,000) and was used to evaluate the susceptibility of 304L stainless steel to pitting corrosion under static, laminar and turbulent flow conditions. Work by Ohio University [27-29] demonstrated the application of a thin channel flow cell (TCFC) for studying corrosion of carbon steel in oil and gas environments under single phase flow scenarios. Here, the test section of the cell is 600 mm long, with a cross section of 3 mm high by 89 mm wide. The system has a solution reservoir of 150 L and is able to generate flow rates through the channel of up to 17 m s^{-1}. The TCFC test section has four ports which are used to flush-mount plug-in probes to measure combinations of differential pressure, wall shear stress and corrosion (via electrochemical probes or mass-loss specimens).

Schlumberger-Private

Recent work has also seen the application of microfluidic cells for examining corrosion processes or corrosion product deposition. Examples include the work of Abe et al. [30] who evaluated copper corrosion in laminar flow conditions using a microfluidic channel with a height of 45 µm, a width of 5 mm and a length of 20 mm. In addition, McGrady et al. [31] have recently reported the development of a microfluidic setup to study the deposition of chalk river unidentified deposits within the water circuits of nuclear reactors.

Certainly, the last two decades have demonstrated a significant increase in the complexity and novelty of flow cell systems to interpret corrosion/deposition mechanisms in industrial processes, with the incorporation of in situ techniques. These include the integration of time lapse microscopy [32], atomic emission spectroscopy [33], X-ray adsorption spectroscopy [34], synchrotron X-ray diffraction [35-37] and Raman spectroscopy [38]. Despite the development of numerous flow cells over the years, to the best of the author's knowledge, this is the first once-through system designed to understand the corrosion response of a material subjected to transitions in fluid chemistry from a strong inhibited acid to a brine solution.

In contrast to industry-standard methods [39], which focus on evaluation of corrosion rate under discrete acid concentrations and various test duration, the flow cell technique offers quantification of the progressive corrosion behaviour when corrosion rate is evaluated through a sequence of transitions of fluid composition. In particular, the flow cell technique can be used to study corrosion during acid flowback sequences.

In this paper, details pertaining to the flow cell design are presented, and its performance is modelled in terms of characterising the fluid flow and the fluid-fluid displacement. Experimental results for a model acid flowback system are also presented. The performance of the fluid flow cell is evaluated for a model hydrochloric acid–sodium chloride (HCl–NaCl) solution in the presence of a standard acid corrosion inhibitor, PA [8]. In this system, a low carbon steel is initially exposed to inhibited 4 mol L^{-1} hydrochloric acid containing 0.05 wt.% PA. The inhibition efficiency of PA changes as the inhibited acid is progressively diluted by an uninhibited 4 mol L^{-1} NaCl solution, which simulates the formation brine. Thus, the steel specimen and inhibitor film experiences concomitant changes in the "external" concentrations of acid and PA whilst the chloride concentration remains constant throughout the experiment.

Schlumberger-Private

2. Experimental procedure

2.1 Materials

HS80^{TM} steel was the material used for all mass-loss tests and electrochemistry experiments. HS80^{TM} is a low carbon steel with a ferrite/pearlite microstructure (shown in Fig. 1) and composition as shown in Table 1. Analytical reagent grade 4 mol L^{-1} HCl, NaCl, and PA were obtained from Sigma-Aldrich.

	C (wt.%)	Mn (wt.%)	P (wt.%)	S (wt.%)	Si (wt.%)	Cr (wt.%)	Cu (wt.%)	Ni (wt.%)	Fe (wt.%)
Manufacturer specification [40]	0.16 max.	1.2 max.	0.02 max.	0.005 max.	0.5 max.	0.45-0.7	0.40 max.	0.25 max.	96.8-97.0
Ranges by XRF analyses of edges and face of sheet	not determined	0.75-0.79	not determined	not determined	0.40-0.52	0.56-0.58	0.27-0.30	0.12-0.15	96.8-97.0

Table 1: HS80^{TM} elemental composition provided by the manufacturer Tenaris [40] and obtained by X-ray fluorescence (XRF) analysis. The HS80^{TM} flat sheet was analysed using an XRF analyser Niton XL2 980 GOLDD – the range of values given by analysis encompass both the edges and faces (each mirror-polished) of the HS80^{TM} sheet.

INSERT FIGURE 1

2.2 Experimental methodology

Static mass-loss experiments were conducted to enable comparisons to be drawn with the flow cell results during different stages of the dilution process. The methodologies implemented for mass-loss and electrochemistry (in both the static system and the flow cell itself) are provided in the following sections.

2.2.1. Mass-loss test methodology

Specimens were prepared by cutting 29±3 cm^2 coupons from HS80^{TM} steel sheets. Before each experiment, specimens were wet-ground using 1200-grit silicon carbide (SiC) paper, degreased with acetone, rinsed with distilled water, and dried gently with compressed air.

For each experiment, the specimen was placed in a glass beaker (with a sealed lid and a condenser) that contained 1 L of a fixed concentration of acid and inhibitor. Tests were performed in HCl solutions of varying concentration to simulate different stages of the HCl–NaCl dilution process. These solutions were prepared by mixing 4 mol L^{-1} HCl (containing 0.05 wt.% PA) at an appropriate ratio with 4 mol L^{-1} uninhibited NaCl brine. Before immersion of the test coupon, the solution was heated to 80℃, and the mass-loss specimen dimensions and mass were taken. Throu ghout

Schlumberger-Private

the experiment, the test solution was continuously stirred using a magnetic stirrer bar to agitate the solution, but caution was taken to prevent any hydrodynamic effects on the steel surface. No effort was made to remove dissolved oxygen from the solution, and all experiments ran for 3h in total. At the end of each 3h experiment, the specimen was removed from the test solution, rinsed with acetone and any residual inhibitor and corrosion deposits were removed by scrubbing with soap and water. Specimens were then rinsed with distilled water and acetone before being dried with compressed air in accordance with the test procedure followed by Barmatov et al. [9, 41]. The specimen was then reweighed. The determined mass-loss was converted into a corrosion rate expressed, V_c, in g m^{-2} h^{-1} based on the dimensions of the specimen prior to exposure to the test solution and using Eq. (1):

$$V_C = \frac{W}{At} \tag{1}$$

where W is the mass loss in g, A is the total area of all the exposed surfaces of the metal coupon in m^2 and t is the immersion time in hours.

The HCl concentrations evaluated were 4 mol L^{-1} (100%), 0.6 mol L^{-1} (15%), 0.04 mol L^{-1} (1%), 0.004 mol L^{-1} (0.1%), and 0.0004 mol L^{-1} (0.01% of original acid content), all made by combining the inhibited 4 mol L^{-1} HCl with different volumes of 4 mol L^{-1} NaCl brine. The corrosion rates of the carbon steel in these different solutions was determined in the presence of PA. An important aspect to note here is that the PA concentration was 0.05 wt.% per litre of 4 mol L^{-1} acid used to create the test solution in each experiment, i.e. the PA concentration remained proportional to the total acid concentration of the system for all experiments. The purpose behind this was to simulate different stages of the flowback process wherein both the acid and inhibitor are progressively diluted with formation brine as a function of time. The acid concentrations and the volume of PA inhibitor used for each of the different experiments are provided in Table 2.

HCl concentration (mol L^{-1}) for HCl–NaCl solution)	**PA (µL) used in experiment to maintain 0.05 wt.% per litre of 4 mol L^{-1} HCl**
4 (100%)*	540
0.6 (15%)	81
0.04 (1%)	5.4
0.004 (0.1%)	0.54
0.0004 (0.01%)	0.054

* Percent of original 4 mol L^{-1} acid concentration (degree of dilution) is shown in parentheses.

Table 2: Molar acid concentrations of HCl–NaCl solution and PA inhibitor volumes formulated for use in the static mass-loss and static electrochemical tests to achieve a constant relative inhibitor concentration of 0.05 wt.% per

Schlumberger-Private

litre of 4 mol L^{-1} HCl. Total chloride concentration of HCl–NaCl solutions was 4 mol L^{-1}.

2.2.2 Electrochemistry test methodology

2.2.2.1 Static closed vessel measurements

In addition to the mass-loss tests, electrochemistry specimens were also used to measure the corrosion rates associated with different inhibited HCl–NaCl solutions in the static environment. Test conditions and solution preparation were identical to those performed in the mass-loss methodology, except that two electrochemistry specimens with an exposed surface area of 1 cm² each were inserted into the test solution. In addition, one larger mass-loss specimen was also positioned in the beaker to maintain a comparable volume-to-surface-area ratio with the mass-loss experiments.

An electrical connection was achieved by soldering a copper wire to one side of the 1 cm^2 specimens before mounting each specimen separately in a non-conducting semi-transparent, low-odour acrylic. The acrylic consisted of a liquid (primarily 2-methyl(tetrahydro-2-furanyl)methyl-2-propenoate and hydroxypropylmethacrylate) and powder (predominantly poly(ethylmethacrylate)) mixture, which yielded an 8-min cure time once combined. After the acrylic had suitably hardened, specimens were wet-ground with 1200-grit SiC abrasive paper, degreased with acetone, rinsed with distilled water, and dried with compressed air prior to insertion into the test solution. No adverse reaction between the acrylic and the HCl was observed in any experiment.

In conjunction with the two carbon steel working electrodes and mass-loss specimen, a 4 mol L^{-1} Ag/AgCl reference electrode was used alongside a platinum counter electrode to form a standard three-electrode cell. The open circuit potential (OCP) of the specimens was monitored and allowed to stabilise for the first 5 min, after which linear polarisation resistance (LPR) measurements were performed on each of the two working electrodes in turn, i.e. performing sequential measurements on each specimen. Each working electrode was polarised ±10 mV from the OCP at a scan rate of 0.25 mV s^{-1}. LPR measurements were performed on each specimen every 15 min over the duration of the 3h test.

In all experiments, the solution resistance, R_s (ohm cm^2) was determined after LPR measurements were complete using electrochemical impedance spectroscopy (EIS). This consisted of polarising the specimen ±5 mV relative to the OCP using a frequency range from 20 kHz to 0.1 Hz. The value of R_s was subtracted from polarisation resistance, R_p (ohm cm^2), to produce a charge-transfer resistance, R_{ct} (ohm cm^2), which was used to determine the corrosion rate behaviour with time:

$$R_{\mathrm{ct}} = R_{\mathrm{p}} - R_{\mathrm{s}} \quad (2)$$

The solution resistance was determined to range between 0.6–1.3 ohm cm^2 across all experiments.

Schlumberger-Private

In addition to LPR and EIS, potentiodynamic measurements were also performed on each specimen at the end of the 3h test in every fixed HCl concentration static experiment. This technique was used to generate Tafel polarisation curves to determine the anodic and cathodic Tafel constants (β_a and β_c, respectively, in mV decade^{-1}) and ultimately an appropriate Stern-Geary coefficient (B) to enable calculation of corrosion rates from the values of R_{ct} determined as a function of time in each experiment. Anodic and cathodic Tafel polarisation plots (plotted as E-log i) were generated by polarising from the OCP to either +100 or -200 mV at a scan rate of 0.5 mV s^{-1}. The cathodic sweep was generated first, before switching to the second electrochemical specimen to generate the anodic Tafel plot.

From the polarisation curves produced, it was possible to determine β_a and β_c by measuring their respective gradients over regions where linearity was observed between the applied voltage and the log of the measured current. The Tafel slope measurements were used to determine the Stern-Geary coefficient in mV decade^{-1}, and the corrosion current density, i_{corr} (mA cm^2):

$$B = \frac{\beta_a \beta_c}{2.303(\beta_c - \beta_a)} \tag{3a}$$

$$i_{corr} = \frac{B}{R_{ct}} \tag{3b}$$

2.2.2.2 Once-through flow cell measurements

In the case of flow cell electrochemical measurements, LPR measurements were performed every 5 minutes using the same three-electrode setup and procedure outlined for static experiments. However, an average value of the Stern-Geary coefficient (determined from all static experiments) was applied to the entire fluid transition response to convert the measured resistances into corrosion current densities using Equations (3a) and (3b). No Tafel measurements were performed in the flow cell itself as excessive polarisation at such low flow rates promoted concerns regarding the stability of the solution chemistry within the cell.

In the context of the flow cell measurements, the assumption of an average Stern-Geary coefficient across the entire fluid transition process to determine in situ corrosion current densities has inherent limitations. However, these values have been provided in order for the results to be easily comparable and translatable across each experiment, and to illustrate the magnitude of the corrosion current densities observed. That being said, values of the reciprocal of charge-transfer resistance are also provided within this publication in conjunction with the corrosion current densities to provide a more accurate representation of the instantaneous corrosion response of the steel surface from an electrochemistry perspective during fluid transitions.

Schlumberger-Private

3. Flow cell design and test methodology

3.1. Cell components and integration with electrochemistry

To determine the instantaneous corrosion rate in progressively diluted HCl–NaCl solutions, a new test methodology is required. This prompted the development of a combined flow cell and “once -through” system that could acquire corrosion measurements by electrochemical methods during the progressive dilution process, reduce the number of experiments required, and exhibit a better tolerance to acid consumption during long-term measurements.

A custom flow cell was designed to accommodate a carbon steel specimen with an exposed area of 1 cm^2, complete with a platinum counter electrode and a 4 mol L^{-1} Ag/AgCl reference electrode. The purpose of the cell design was to enable a fresh acid/inhibitor mixture to be delivered through the cell in a once-through fashion. The intention was that this acid mixture could be progressively diluted over time with 4 mol L^{-1} NaCl electrolyte to model acid flowback in one single experimental run. Through the integration of a three-electrode cell, real-time electrochemical measurements can be performed to determine how the corrosion rate of the steel specimen changes during flowback whilst also avoiding the complications associated with both acid/inhibitor spending and solution contamination.

Fig. 2 outlines the geometry of the test cell, which consists of a top (1) and a bottom block (2) manufactured from highly acid resistant polyethylene and held together with 10 M6 nuts and bolts (3). Inlet and outlet ports are positioned in the bottom section of the cell (4). The carbon steel specimen is flush mounted into the base of the cell and sealed in with a non-conducting acid resistant resin with strong edge retention to prevent crevice corrosion of the coupon (5). An electrochemical connection to the steel specimen is facilitated by soldering a wire to the back of the steel specimen before mounting in resin. The platinum counter electrode and Ag/AgCl reference electrode were both flush mounted into the top of the cell directly opposite from the carbon steel specimen (6). Research by Taylor and Nieman [42] as well as Myland and Oldham [43] has shown that positioning the working electrode directly opposite the reference and counter electrodes within such a flow cell is the best configuration to minimise both noise and solution resistance. The top and bottom block are separated using a custom laser-cut gasket of thickness 2 mm, manufactured from Viton FKM (7).

INSERT FIGURE 2

3.2. Selection of gasket geometry

The choice of geometry for the flow cell gasket was extremely important. Although the fluid flow in the system is laminar, regions of reversed fluid motion (or eddies) can still develop in the system as the flow channel expands. It is imperative to prevent the formation of eddies within the system and to ensure that any “fresh” acid/inhibitor entering the system exits the flow cell quickly once it has passed over

Schlumberger-Private

the steel surface. The build-up of reacted acid/inhibitor within the cell would result in an inaccurate simulation of the flowback process, producing misleading results. Failure to fully understand the behaviour of fluid flow along with the advection and diffusion processes within the cell would result in a poorly designed cell that fails to simulate the once-through process.

The flow cell geometry was chosen based on the findings from a study by Pike et al. [44]. Their research focused on the evaluation of a number of central flow cell channel designs for biosensor applications and concluded that the most efficient geometry (i.e. the gasket geometry, which delays the onset of eddy development towards higher velocities) was that termed the iCell (named due to its similarity to the shape of an eye). The geometry of the cell is actually specified via a third-order polynomial. One-quarter of the profile is provided by the local x, y coordinate positions (in mm) $y = (C_1x^3 + C_2x^2 + C_3x + 0.5)$, $(0 \leq x \leq 9)$ with $C_1 = -(2b/a^3)$, $C_2 = (3b/a^2)$, and $C_3 = 0$, and subject to the size constraints in this instance given by a = 18 mm and b = 12 mm. This curve was reflected about the vertical and horizontal planes to give the final geometry of the central part of the flow cell, as shown in Fig. 3. The thickness of the gasket within this system was set at 2 mm.

INSERT FIGURE 3

3.3. Numerical and experimental validation of flow cell

3.3.1. Setup of numerical model and input parameters

To validate the design of the flow cell from the perspective of preventing depletion of H^+ ions and accumulation of Fe^{2+} ions within the cell, both a computational and an experimental approach were employed. A three-dimensional geometric model was built to match the constructed flow cell, with the flow domain comprising 460,000 elements (determined by creating a progressively finer mesh until a robust, mesh-independent solution was obtained for both the flow domain and the concentration gradients of species from the steel surface). A distributed boundary-layer mesh was also implemented at the wall of the steel specimen to adequately resolve the concentration gradients as a result of the simulated corrosion process. The constructed geometry and optimised mesh are shown in Fig. 4.

INSERT FIGURE 4

The behaviour of the flow cell was studied within COMSOL Multiphysics using the standard time-dependent advection-diffusion equation for an incompressible flow:

$$\frac{\partial c}{\partial t} = D\boldsymbol{\nabla}^2 c - \mathbf{u} \cdot \boldsymbol{\nabla} c \qquad (4)$$

where c is concentration, t is time, D is the diffusion coefficient, $\mathbf{u}$ is velocity field; and $\boldsymbol{\nabla}$ is the del operator.

Schlumberger-Private

Prior to solving the concentration, the velocity field was established by solving the steady-state Navier-Stokes equation for an incompressible fluid under laminar conditions:

$$\rho(\mathbf{u} \cdot \boldsymbol{\nabla}\mathbf{u}) = -\boldsymbol{\nabla}p + \mu\boldsymbol{\nabla}^2\mathbf{u} \quad (5a)$$

$$\boldsymbol{\nabla} \cdot \mathbf{u} = 0 \quad (5b)$$

where ρ is fluid density, p is fluid pressure, and μ is the dynamic viscosity.

The boundary conditions associated with the flow were chosen to be representative of the flow cell dilution experiment. A symmetry boundary condition was used to reduce the computational effort. The physical properties of the fluid were defined based on the concentration of the acid travelling through the cell and were set to match those recorded in previous studies [9].

Full details of chemical properties of the fluid within the flow cell are provided in Table 3. The density and viscosity were calculated using a law of mixtures to find values for the mixed solution based on density values of 1044.6 kg m^{-3} and 1205.6 kg m^{-3} and viscosity values of 3.475x10^{-4} Pa.s and 3.54x10^{-4} Pa.s for the 4 mol L^{-1} HCl and NaCl solutions at 80ºC, respectively [45]. Initial concentrations of species were based on the molarities entering the cell, as shown in Table 2 (values ranging from 4 mol L^{-1} to 4x10^{-4} mol L^{-1}) whilst also accounting for the presence of H^+, $Cl^–$, Na^+ and $OH^–$ ions. The corrosion rate used to model the Fe^{2+} and H^+ flux was defined in terms of surface fluxes where 0.0863 mA cm^{-2} of corrosion current density (equal to 1 mm $year^{-1}$) equated to 4.47x10^{-6} mol m^{-2} s^{-1} flux of Fe^{2+} from the surface and 8.94x10^{-5} mol m^{-2} s^{-1} flux of H^+ into the surface. The equations were solved using the finite element method within the COMSOL Multiphysics simulation package.

Schlumberger-Private

Property Name/Symbol	Expressions	Description
K_{H2O}	$10^{-(29.3868-0.0737549T+7.47881\text{x}10^{-5}T^2)}$ mol^2 m^{-6}	Water dissociation constant [46]
$k_{H2O,\,b}$	7.85x10^7 m^3 (s mol)$^{-1}$	Backward rate constant for dissociation of water [46]
D_{cH}	9.312x10^{-9} m^2 s^{-1}	Diffusion coefficient of hydrogen ions [46]
D_{cFe}	0.72x10^{-9} m^2 s^{-1}	Diffusion coefficient of iron ions [46]
D_{cCl}	2.032x10^{-9} m^2 s^{-1}	Diffusion coefficient of chloride ions [46]
D_{cOH}	5.26x10^{-9} m^2 s^{-1}	Diffusion coefficient of hydroxide ions [46]
D_{cNa}	1.334x10^{-9} m^2 s^{-1}	Diffusion coefficient of sodium ions [46]
(Note: T is temperature in degrees Kelvin. Molecular diffusion coefficients are reference coefficients. Each specific molecular coefficient is determined using $D_{\mathrm{i}} = D_{\mathrm{ref}}\frac{T}{T_{\mathrm{ref}}}\frac{\mu_{\mathrm{ref}}}{\mu}$, where the subscript ref denotes reference values at 20^{o}C; i.e. T_{ref} = 293K and μ_{ref} = 1.002x10^{-3})		

Table 3: Chemical properties of acid/brine mixtures defined for the purpose of simulating diffusion processes and chemical equilibrium reactions occurring within the flow cell using COMSOL Multiphysics.

3.3.2. Numerical model flow rate results

Initially, an analysis of the velocity field within the flow cell was performed to determine the upper limits of flow rate within the cell. Flow rates ranging from 1 ml min^{-1} to 25 ml min^{-1} were simulated, and a selection of results are provided in Fig. 5.

The images displayed on the left hand side of Figures 5(a) to (c) indicate the velocity field under different simulated flow rates of 1, 10, and 25 ml min^{-1}. The right hand side images in the same figures indicate the velocity profile across the leading edge, trailing edge, and centre of the steel specimen at a distance of 1 mm from the surface of the specimen (i.e., the midpoint of the gasket). The purpose of this is to be able to clearly identify regions within the cell where flow across the specimen is non-uniform, recirculating, or stagnant. The dimensions of the square carbon steel specimen embedded into the base of the flow cell are provided in each of the images to show the distribution in fluid velocity as it passes over the surface of the specimen. At a flow rate of up to 15 ml min^{-1}, the velocity field was observed to be constant over the specimen and the velocity profile across the specimen was more uniform than at the higher flow rate of 25 ml min^{-1}. Based on this analysis, the maximum flow rate was defined as 15 ml min^{-1}. Although higher flow rates would be permissible without resulting in recirculation of the fluid, a non-uniform velocity profile would be achieved over the specimen surface at flow rates in excess of 15 ml min^{-1}.

INSERT FIGURE 5

Schlumberger-Private

3.3.3. Numerical model corrosion simulation results

The final validation within the model was to ensure that as the steel specimen corroded, the corrosion kinetics were not so fast that they caused a build-up of reacted acid within the cell and that Fe^{2+} ions did not accumulate, influencing the response of the electrochemical measurements.

In the next stage of numerical simulation, after solving the steady-state flow equations, the advection-diffusion process is solved subject to the determined velocity field for inlet flow rates of 1, 5, 10, and 15 ml min^{-1}, using the diffusion coefficients specified in Table 3. The concentration of HCl entering the cell was varied by orders of magnitude from 4 mol L^{-1} down to 0.0004 mol L^{-1}. All walls were constrained to zero flux with the exception of the surface representing the carbon steel specimen. For this surface, a positive flux of Fe^{2+} ions and a negative flux of H^{+} ions was specified. Corrosion current densities chosen for the steel specimen ranged from 86.3 mA cm^{-2} (intended to represent a worst case scenario based on the work of Barmatov et al. [9] who reported uninhibited acid corrosion rates of the order of 1000 mm $year^{-1}$) down to 0.0863 mA cm^{-2} to establish the operating limits within the cell (based on acid spending). However, specific corrosion rates relating to those recorded in static conditions (shown later in Table 5) were also defined to compare the extent of acid spending in the static system with the flow cell under comparable chemistries. The independence of the solution with respect to grid density was confirmed using a progressively finer mesh system to resolve the concentration gradients across the boundary layer of the steel specimen.

Fig. 6 provides an example of the surface concentration maps produced from the numerical model. These images depict the concentration of H^{+} and Fe^{2+} ions across the surface of the steel specimen within the flow cell at the lowest flow rate 1 ml min^{-1} and the highest acid concentration 4 mol L^{-1} and corrosion current density of 86.3 mA cm^{-2} (simulating an extreme, but realistic, corrosion rate under uninhibited conditions [9]). The image shows clearly that the reacted acid and produced Fe^{2+} ions do not accumulate within the cell, even in the absence of inhibitor.

INSERT FIGURE 6

In relation to acid consumption within the flow cell, this effect is minimised significantly due to the once-through nature of the flow process and the smaller specimen geometry as compared to standard mass-loss testing under static conditions. The corrosion current density of carbon steel can approach 86.3 mA cm^{-2} in uninhibited 4 mol L^{-1} HCl at 80^{o}C. In this situation, a static test with a 29 cm^2 specimen in a 1 L solution for 3h would consume approximately 7.0% of the acid. This could rise to over 35% if a 200 ml solution is used as in some other studies [9]. This can be a significant problem as acid consumption leads to a lower cumulative mass-loss, which may result in a poor estimation of inhibitor efficiency. The results of the flow cell simulations indicate that, in 4 mol L^{-1} HCl with a corrosion current density of 86.3 mA cm^{-2}, at flow rates of 1, 5, 10, and 15 ml min^{-1}, acid consumption levels are 1.34, 0.27, 0.13, and 0.09%, respectively. These values are significantly

Schlumberger-Private

lower than those for standard mass-loss testing under static conditions, and they can be regarded as a quasi-stationary state.

To assist in determining the limits of operation of the flow cell more precisely, based on consumption rates across different acid concentrations, a series of calculations were performed. The maximum corrosion current density tolerable at the steel surface for a specific percentage of acid consumption within the cell can be determined by considering the flow rate through the system. Firstly, the number of moles of H^+ travelling through the cell per unit time can be defined as:

$$j_{H^+} = Q[\mathrm{H^+}] \tag{6a}$$

where $j_{H^+}$is the flux of H^+ through the cell in mol s^{-1}, Q is the solution flow rate through the cell in L s^{-1} (noting that 1 ml min^{-1} is equivalent to $\frac{1}{60000}$ L s^{-1}), and $[H^+]$ is the acid concentration flowing through the cell in mol L^{-1}.

Multiplying $j_{H^+}$by P, the percentage of acceptable depletion (expressed as a decimal) produces the maximum acceptable rate of H^+ consumption at the steel surface ($j_{H^+,s}$):

$$j_{H^+,s} = P j_{H^+} \tag{6b}$$

$j_{H^+,s}$ can then be converted into a maximum tolerable corrosion current density at the steel surface, $i_{corr,\,tol}$, in A m^{-2} using:

$$i_{corr,tol} = \frac{nF j_{H^+,s}}{A} \tag{6c}$$

where n is the number of electrons exchanged in the reaction for every mole of H^+ reacting at the steel surface (1), F is the Faraday constant (coulomb mol^{-1}) and A is the steel surface area (0.0001 m^2). $i_{corr,tol}$ can be converted into units of mA cm^{-2} through multiplication of the current density in A m^{-2} by 0.1.

Table 4 provides an example of tolerable corrosion current densities (in mA cm^{-2}) over a wide range of acid concentrations and cell flow rates for a consumption of 1% acid in each scenario. The table demonstrates that a wide range of flow rates are tolerable within the cell without significantly depleting the acid content in the system.

Schlumberger-Private

HCl (mol L^{-1})	Maximum tolerable corrosion rate (mA cm^{-2}) within the flow cell to remain below 1% HCl consumption			
	1 ml min^{-1}	5 ml min^{-1}	10 ml min^{-1}	15 ml min^{-1}
4	64.3	321	643	967
0.6	9.67	48.3	96.7	145
0.04	0.643	3.21	6.43	9.67
0.004	0.0643	0.321	0.643	0.967
0.0004	0.00643	0.0321	0.0643	0.0967

Table 4: Tolerable specimen corrosion rates within the flow cell across different flow rates and acid concentrations to ensure acid consumption <1%.

A comparison of the actual acid consumption levels between inhibited static and flow cell conditions across all acid contents performed in this study is also provided in Section 4.2. It is also important to stress that in all simulations performed over acid inlet concentrations of 4 mol L^{-1} to 0.0004 mol L^{-1}, a steady-state response was achieved within the cell, and no accumulation of reacted acid or Fe^{2+} was observed.

4. Results and discussion

4.1. Development of acid dilution system and temperature control for flow cell

4.1.1. Description of complete setup

After the design and validation of the flow cell was complete, it was integrated into a system capable of simulating acidizing flowback. Fig. 7 provides a schematic representation of the complete setup. This initially consists of 1 L of 4 mol L^{-1} HCl (containing 0.05 wt.% PA) and 10 L of 4 mol L^{-1} NaCl solution (which was periodically replenished if required) in separate vessels. An ISMATEC® REGLO digital peristaltic pump is used to deliver a controlled flow rate between 1 and 15 ml min^{-1} (with a pump accuracy of ±5%) of NaCl solution from the 10 L container into the 1 L vessel, resulting in a decrease in the acid concentration as a function of time. At the same time, an identical peristaltic pump is used to transfer the solution from the 1 L vessel through the flow cell and into a waste container at the same flow rate. The Tygon® tubing used to transfer both solutions between vessels and to the flow cell was tested for chemical compatibility with 4 mol L^{-1} HCl at 80ºC. A water bath (discussed later) is also used to control the temperature of the solution entering into the flow cell. The full setup ensures gradual dilution of the acid/inhibitor mixture with 4 mol L^{-1} NaCl in a controlled manner.

INSERT FIGURE 7

4.1.2. Temperature control within the flow cell

A water bath was used to regulate the temperature within the flow cell. After the acid/brine mixture leaves the 1 L vessel at room temperature, it travels through

Schlumberger-Private

Tygon tubing immersed in the water bath to heat it to the desired temperature. In addition, the flow cell is immersed in the water bath to ensure no temperature drop occurs whilst the solution is flowing through the cell. The application of the water bath was validated using a customised cell integrated with a thermocouple, and it was found that a temperature of up to 80^{o}C could reliably be reached by controlling the temperature of the water bath to 5^{o}C above the desired temperature.

4.1.3. Control of dilution rates

Within this system, it is possible to control the rate of dilution of the 4 mol L^{-1} acid by varying the speed of the two peristaltic pumps. The change in H^+ molarity of the solution travelling through the flow cell can be expressed by considering the dilution of the second 1 L vessel shown in Fig. 7 using the general dilution equation for a system with a fixed fluid volume [47]:

$$[H^+](t) = [H^+]_0 e^{-\frac{Qt}{V}} \quad (7)$$

where the acid molarity at a given time ($[H^+](t)$) in mol L^{-1} is calculated from the initial acid molarity $[H^+]_0$ in mol L^{-1}, the volume of the acid within the second vessel (V) in L, the time (t) in seconds and the volumetric flow rate (Q) in L s^{-1}. This equation requires the assumption that the H^+ molarity of the diluting fluid is significantly smaller than that of the fluid being diluted as well as perfect mixing in the second vessel.

A flow rate of 10 ml min^{-1} was used to simulate a typical dilution profile as encountered after production restarts following an acidizing treatment based on the available literature [48]. This rate of dilution required a total solution volume of 12 L over 20h.

4.2. Static experimental results

Example polarisation curves measured across a range of different HCl concentrations (4 mol L^{-1}, 0.04 mol L^{-1} and 4×10^{-4} mol L^{-1}) are provided in Fig. 8. The anodic and cathodic Tafel constants determined for each inhibited acid concentration after 3h for static tests are provided in Table 5 along with the calculated Stern-Geary coefficient for each condition. These were used to convert the electrochemical measurements (R_{ct}) determined using the LPR technique to corrosion current densities. The percentage consumption of acid in each static test as compared with the flow cell at different stages of the dilution process are also provided in Table 5. The calculations and simulations show that the consumption percentage is minimal at all stages of the dilution process in the flow cell (<2%). However, consumption of acid within the static tests is appreciable, particularly at 0.004 mol L^{-1}, reaching in excess of 70%.

INSERT FIGURE 8

Schlumberger-Private

The converted LPR results, along with those of the mass-loss measurements, are provided in Fig. 9, which depicts the average corrosion rate calculated based on at least two repeats using each method. The errors bars for mass-loss indicate the highest and lowest corrosion rates recorded across all individual mass-loss experiments at each condition. The error bars for the electrochemical data correspond to the highest and lowest individual LPR corrosion rates recorded over the entire duration of all 3h experiments at each experimental condition (noting that 12 LPR measurements were performed per test).

HCl, mol L^{-1}	β_a, mV $decade^{-1}$	β_c, mV $decade^{-1}$	Stern-Geary coefficient mV $decade^{-1}$	OCP (vs 4 mol L^{-1} Ag/AgCl) mV	i_{corr}, mA cm^{-2}	Acid consumption in static 3h, %	Equivalent acid consumption in flow cell at 10 ml min^{-1}, %
4	35	-200	13	-387	1.36	0.11	0.0021
0.6	30	-190	11.3	-402	0.906	0.49	0.0094
0.04	60	-120	17.4	-450	1.55	12.54	0.24
0.004	30	-930	12.6	-644	0.958	77.73	1.45
0.0004	30	-480	12.3	-677	0.0518	42.02	0.80

Table 5: Anodic (β_a) and cathodic (β_c) Tafel constants, OCP (vs Ag/AgCl), calculated Stern-Geary coefficient, and acid consumption levels for HS80™ steel observed at the end of 3h static mass-loss experiments across a range of different acid concentrations of HCl–NaCl solutions inhibited with 0.05 wt.% PA (relative to the 4 mol L^{-1} HCl). The equivalent acid consumption if the experiment were to be performed in the flow cell (at 10 ml min^{-1}) is provided for each of the conditions.

Fig. 9 highlights the potential corrosivity of the fluid based on the individual fixed concentration experiments, even when inhibited with PA. The figure shows a comparison between mass-loss measurements (in g m^{-2} h^{-1}) over a period of 3h in the static environment with the average LPR corrosion current densities (in mA cm^{-2}) extract over multiple experiments and also recorded in the same static, closed system. For comparison, it is possible to convert the corrosion current densities into an equivalent mass loss rate for carbon steel using Faraday's Law:

$$V_C = \frac{KM}{nF} i_{corr} \quad (8)$$

where V_c is the mass loss rate expressed in g m^{-2} h^{-1}, i_{corr} is the corrosion current density in mA cm^{-2}, M is the atomic mass of iron in g, n is the number of electrons exchanged in the dissolution reaction, F is the Faraday constant in coulomb.mol^{-1} and K is a constant (K=36000).

Eq. (8) indicated that 1 mA cm^{-2} in the context of steel dissolution in acidic media converts to approximately 10.4 g m^{-2} h^{-1}. Accordingly, the two y-axes in Fig. 9 are

Schlumberger-Private

scaled so that they are directly comparable between both mass lass and electrochemical data.

Considering Fig. 9, the highest average corrosion rate (~18.0 g m^{-2} h^{-1}) from the mass-loss tests was observed at the highest HCl concentration of 4 mol L^{-1} with 0.05 wt.% PA and the least corrosive solution contained the lowest HCl concentration (0.540 g m^{-2} h^{-1} at 0.0004 mol L^{-1} HCl with $5x10^{-5}$ wt.% PA). Overall, there is strong agreement between the LPR measurements and mass-loss data in the static environment, and the results indicate that even at low acid concentrations, the solution can be particularly corrosive in the presence of PA. At concentrations of 0.04 mol L^{-1} and 0.004 mol L^{-1} HCl, the H^+ concentrations are 100 and 1000 times lower than the initially injected acid, yet the corrosion rate is in excess of 8.99 g m^{-2} h^{-1}. Despite the large difference in HCl concentration, the change in corrosion rate is small between these different HCl molarities, suggesting that dissolution rate is significant well into the latter stages of the flowback process. The high corrosion rates at significantly lower HCl concentrations can be explained by the fact that the associated PA concentrations are also 100 and 1000 times lower than the initial concentrations for the 0.04 mol L^{-1} and 0.004 mol L^{-1} HCl solutions, respectively. The results of these experiments are useful for comparison with results from different stages of the flow cell experiment, as discussed later.

INSERT FIGURE 9

The results in Fig. 9 require careful consideration because both the inhibitor and acid concentrations vary between each experiment as a result of the acid-to-inhibitor ratio being maintained at 0.05 wt.% PA per litre of 4 mol L^{-1} HCl used to formulate each solution. It is clear that this results in somewhat unpredictable corrosion behaviour across these conditions, i.e. the corrosion rate does not simply decrease with acid content when inhibited by PA in this system.

It is important to understand that the 3h static mass-loss tests are designed to evaluate the corrosivity of the injected fluid (with a constant acid and inhibitor concentration) and not to assess corrosion during flowback. For the latter, the main limitation of the 3h static test methodology is that in each experiment, the acid and inhibitor concentrations are constant throughout the test. Therefore, such tests can only assess corrosion behaviour at one instant in time during flowback. That being said, the initial static test results in Figure 9 show an interesting trend in corrosion rate at different stages of flowback. They indicate that when both PA and HCl concentration reduce proportionally over time, the corrosion rate does not reduce proportionally with acid concentration. However, to fully characterise the transient response of the carbon steel corrosion rate during flowback, a potentially large and impractical number of fixed acid/inhibitor tests is needed, requiring significant materials and labour expenditures.

The application of the flow cell presented here enables quantification of the full flowback corrosion profile and eliminates any issues surrounding acid/inhibitor depletion. The setup also accounts for the history effect imparted on the steel by the

Schlumberger-Private

flow of the preceding fluid. The corrosion induced by the history of the previous fluid chemistry affects the condition of the steel surface which, in turn, can potentially alter the adsorption characteristics of the inhibitor and its efficiency [49, 50].

4.3. Flow cell results

The flow cell tests were conducted at 80°C, starting with 4 mol L^{-1} HCl containing 0.05 wt.% PA inhibitor and progressively diluted with uninhibited 4 mol L^{-1} NaCl brine. Each test was repeated at least twice to ensure accurate and reliable results. The flow rate chosen for the experiment was 10 ml min^{-1} because this produced a rapid change in acid concentration. Such a response was considered to produce the highest variability with regards to the acquisition of electrochemical measurements over time whilst also replicating a typical acid concentration profile encountered in the field based on the reviewed literature [48].

Electrochemical measurements were performed every 5 min using the LPR technique, and the OCP was measured between polarisation tests (the variation in OCP and the reciprocal of the charge-transfer resistance over the duration of the flow cell test is shown in Figures 10(a) and 10(b), respectively, alongside the average values determined over the course of the 3h static electrochemical tests). These charge-transfer resistance values were subsequently converted to corrosion current densities using the Stern-Geary equation. The Stern-Geary coefficient was evaluated in static corrosion experiments at fixed acid concentrations and shown to vary between approximately 12 and 17 (referring back to Table 5) over acid concentrations from 4 mol L^{-1} down to $4x10^{-4}$ mol L^{-1} HCl in the presence of 0.05 to $5x10^{-6}$ wt.% PA (depending upon acid concentration). The average Stern-Geary coefficient across all static tests was found to be 13.3. The corrosion rate response when this Stern-Geary coefficient was applied is shown in Fig. 11 in conjunction with the static data. The corrosion current densities shown in Fig. 11 are, however, only an approximation because it is unknown to what extent the Stern-Geary coefficient varies over the duration of the dilution test. The static mass loss data included in Fig. 11 is also represented in the form of corrosion current densities through the application of Eq. (8) to enable comparison across all measurements.

INSERT FIGURE 10

A number of key observations can be made from the results shown in Figures 9 and 10. First, the corrosion rate does not continuously decrease proportionally with the concentration of hydrochloric acid in the HCl–NaCl solution when in the presence of PA. As acid concentration reduces in the early stages of the experiment, the corrosion rate actually increases, with two peaks in corrosion current density when the solution contains $2x10^{-2}$ mol L^{-1} and $8x10^{-3}$ mol L^{-1} HCl, agreeing with the observed static data.

Second, although the OCP of the steel continuously decreases over the course of the first 16h (Fig. 10(a)), the corrosion rate both rises and declines over this period, suggesting shifts in both the anodic and cathodic reactions occur throughout the

Schlumberger-Private

duration of the experiment. Finally, the shape of the corrosion curve has good reproducibility from the results of two replicate experiments.

INSERT FIGURE 11

As stated previously, the corrosion rates obtained from the 3h static tests are also plotted in conjunction with the dilution test results in Fig. 11. To enable a direct comparison, the 3h static mass-loss and static LPR corrosion current densities are plotted at the corresponding times where the solution passing through the flow cell is at an equivalent HCl and PA concentration. Comparison of the static results and the dilution tests in Fig. 11 indicates that the corrosion rates are comparable (i.e., corrosion rate falls, before increasing to a peak, before a decline towards “normal” production corrosion rates).

However, one distinct difference is that in the dilution tests, the corrosion rate of the specimen is noticeably higher that that predicted by the static corrosion experiment at a 0.04 mol L^{-1} HCl concentration. This could be attributed to the initial adsorption influencing the subsequent response of the surface. Alternatively, given the high corrosion rates of the steel surface, the exposure of iron carbide (Fe_3C and a C-rich phase formed by acid hydrolysis of cementite) and the development of a corroded surface may accelerate corrosion and change the adsorption characteristics of PA [50]. Another potential explanation for the discrepancy is that the reproducibility of the static tests is poor at this particular concentration due to the erratic nature of the corroded metal surface and poor efficiency of the inhibitor at this dosage. Finally, it is also important to note that (i) the Tafel values were shown to vary depending upon the static solution chemistry and (ii) acid or inhibitor consumption within the static cell may also have played a role.

The results indicate that the flow cell can be used to model some critical aspects of the acid flowback process. Initially, during acid injection, the steel surfaces are exposed to strong acid containing a high inhibitor concentration. During flowback, unspent acid containing inhibitor is in contact with exposed surfaces, but this is progressively displaced by formation brine without inhibitor. The flow cell technique can be used to quantify progressive corrosion during this displacement process. The dilution rate within the flow cell can be controlled to simulate different rates of flowback after different acidizing treatments. This can assist in optimising the flowback process both in terms of maximising production and minimising corrosion. The flow cell can also be used to study the effect of changing a range of other parameters including the metal/alloy type, the ionic composition of the formation brine (e.g., presence of calcium, magnesium, bicarbonate, etc.), the presence/absence of CO_2, and presence/absence of different inhibitor chemistries and dosages.

Schlumberger-Private

5. Conclusions

A new experimental technique is introduced that is able to model the progressive corrosion behaviour of a metal surface encountered during acid flowback after matrix acidizing treatments. The once-through flow cell system is designed, optimised, and integrated with electrochemistry, enabling a steel specimen to be initially exposed to an inhibited acid (simulating unspent acid) that is subsequently diluted by an uninhibited brine solution (simulating formation brine), all whilst being monitored for real-time corrosion rates.

The flow cell can withstand 80ºC 4 mol L^{-1} HCl solution and can model different rates of well recovery from acidizing procedures, ranging from <10h to in excess of 2 days. In principle, the technique can be applied to any given acid flowback scenario wherein a metal surface is exposed to a sequence of acid flowback fluids including the post-flush, the partially spent main acid stage, the pre-flush, and the formation brine.

In this paper, experiments are performed for a model flowback system where a low carbon steel is exposed to 4 mol L^{-1} hydrochloric (HCl) with 0.05 wt.% PA inhibitor to generate a polymeric film. The inhibited acid is then progressively diluted using 4 mol L^{-1} NaCl to maintain a constant chloride concentration. This sequence can be considered one of the simplest models of the acid flowback process. The inhibition efficiency of the film and the steel corrosion rate were observed to change significantly during the dilution (flowback) process as the inhibitor film experiences concomitant changes in external concentrations of both acid and PA inhibitor. Most importantly, the corrosion rate of the steel specimen within the flow cell did not decay linearly or exponentially with acid content, highlighting the important role of inhibition within the system. Additionally, the OCP of the steel surface reduced throughout the duration of the experiment, despite the corrosion rate both declining and rising, indicating the complex variation in both anodic and cathodic reactions during dilution.

The experimental results from the flow cell were also compared with various short duration (3h) industry standard static tests in which the solution chemistry was controlled at fixed concentrations to mimic different instances in time during the flow cell dilution process. The flowing system brings the benefit of eliminating acid spending, which was evident in some of the static experiments performed. Furthermore, results show that the new methodology is able to effectively capture the dynamics of the flowback process, producing a repeatable, full corrosion rate profile during flowback.

6. Acknowledgments

The authors would like to acknowledge the financial sponsorship provided by EPSRC studentship funding and Schlumberger.

Schlumberger-Private

The raw/processed data required to reproduce these findings cannot be shared at this time as the data also forms part of an ongoing study.

7. References

[1] M.J. Economides, K.G. Nolte, Reservoir stimulation, Wiley, Chichester, England; New York, 2000.

[2] B.B. Williams, J.L. Gidley, R.S. Schechter, Acidizing Fundamentals, Henry L. Doherty Memorial Fund of AIME, Society of Petroleum Engineers of AIME, 1979.

[3] S.A. Ali, L. Kalfayan, C.T. Montgomery, Acidizing, SPE, 2016.

[4] S. Al-Harthy, Oscar Bustos, Matthew Samuel, John Still, Michael J. Fuller, Nurul Ezalina Hamzah, Mohd Isal Pudin bin Ismail, A. Parajat, Options for high temperature well stimulation, Oilfield Review, 20 (2008).

[5] C.W. Crowe, Prevention of Undesirable Precipitates from Acid Treating Fluids, in: International Meeting on Petroleum Engineering, Society of Petroleum Engineers, Beijing, China, 1986.

[6] R.D. Gdanski, C.E. Shuchart, Advanced Sandstone-Acidizing Designs With Improved Radial Models, SPE Production & Facilities, 13 (1998).

[7] R.L. Hartman, B. Lecerf, W.W. Frenier, M.E. Ziauddin, H.S. Fogler, Acid-Sensitive Aluminosilicates: Dissolution Kinetics and Fluid Selection for Matrix-Stimulation Treatments, SPE Production & Operations, 21 (2006).

[8] M. Finšgar, J. Jackson, Application of corrosion inhibitors for steels in acidic media for the oil and gas industry: A review, Corrosion Science, 86 (2014) 17-41.

[9] E. Barmatov, J. Geddes, T. Hughes, M. Nagl, Research On Corrosion Inhibitors For Acid Stimulation, in: Corrosion, NACE International, Salt Lake City, UT, 2012.

[10] R.J. Tedeschi, Acetylenic Corrosion Inhibitors, Corrosion, 31 (1975) 130-134.

[11] W.W. Frenier, Hill, D.G. and Jasinski, R, Corrosion inhibitors for acid jobs, Oilfield Review, 1 (1989).

[12] W.W. Frenier, F.B. Growcock, V.R. Lopp, Mechanisms of Corrosion Inhibitors Used in Acidizing Wells, SPE Production Engineering, 3 (1988) 584-590.

[13] G. Trabanelli, F. Zucchi, G. Brunoro, G. Rocchini, Corrosion inhibition of carbon and low alloy steels in hot hydrochloric acid solutions, British Corrosion Journal, 27 (1992) 213-217.

[14] D. Jayaperumal, Effects of alcohol-based inhibitors on corrosion of mild steel in hydrochloric acid, Materials Chemistry and Physics, 119 (2010) 478-484.

[15] B.B. Pati, P. Chatterjee, T.B. Singh, D.D.N. Singh, Effect of Propargyl Alcohol on Corrosion and Hydrogenation of Steel in Hydrochloric Acid Solution, Corrosion, 46 (1990) 354-359.

[16] A. Hayatdavoudi, A. Ghalambor, V. Veludandi, Application of a New Technique in Acid Flowback Analysis, in: SPE Formation Damage Control Symposium, Society of Petroleum Engineers, Lafayette, Louisiana, 1996.

[17] L.N. Morgenthaler, P.R. Rhodes, L.L. Wheaton, Testing the Corrosivity of Spent HCl/HF Acid to 22 Cr and 13 Cr Stainless Steels, in: International Symposium on Oilfield Chemistry, Society of Petroleum Engineers, Houston, Texas, 1997.

[18] K.C. Taylor, H.A. Nasr-El-Din, Flowback Analysis of Acid Stimulation of Seawater Injection Wells: Case Histories, in: SPE International Symposium on Formation Damage Control, Society of Petroleum Engineers, Lafayette, Louisiana, 2000.

[19] M.K. Hashem, H.A. Nasr-El-Din, J.A. Hopkins, An Experience in Acidizing Sandstone Reservoirs: A Scientific Approach, in: SPE Annual Technical Conference and Exhibition, Society of Petroleum Engineers, Houston, Texas, 1999.

[20] S.A. Paige, J. Redder, A.G. Shepherd, New Insights On Acid Stimulation Of Sour Gas Wells With Flowback To Facilities Without Production Test Equipment, in: SPE Annual Technical Conference and Exhibition, Society of Petroleum Engineers, San Antonio, Texas, 2012.

[21] S. Hernandez, L. Goodman, M. Knobles, R.W. Schutz, Materials and Corrosion Risk Mitigation Associated with Flowback of Acid Stimulation Fluids, in: CORROSION 2017, NACE International, New Orleans, Louisiana, 2017.

[22] A.L. Barcarella, A.L. Sutton, Electrochemical Measurements on Zirconium and Zircaloy-2 at Elevated Temperatures II. 200°–300°C, Journal of the Electrochemical Society, (1965) 546-553.

[23] E. Stupnišek-Lisac, N. Galić, R. Gašparac, Corrosion Inhibition of Copper in Hydrochloric Acid Under Flow Conditions, CORROSION, 56 (2000) 1105-1111.

[24] K.E. Duncan, B.M. Perez-Ibarra, G. Jenneman, J.B. Harris, R. Webb, K. Sublette, The Effect of Corrosion Inhibitors on Microbial Communities Associated with Corrosion in a Model Flow Cell System, Applied microbiology and biotechnology, 98 (2014) 907-918.

[25] J. Postlethwaite, R.A. Brierley, Electrochemical Flow Cell for Elevated Temperature/Pressure Aqueous Corrosion Studies, Corrosion Science, 10 (1970) 885-890.

[26] J.A. Wharton, R.J.K. Wood, Influence of Flow Conditions on the Corrosion of AISI 304L Stainless Steel, Wear, 256 (2004) 525-536.

[27] F. Farelas, M. Galicia, B. Brown, S. Nesic, H. Castaneda, Evolution of Dissolution Processes at the Interface of Carbon Steel Corroding in a CO2 Environment Studied by EIS, Corrosion Science, 52 (2010) 509-517.

[28] W. Li, B.F.M. Pots, B. Brown, K.E. Kee, S. Nesic, A direct measurement of wall shear stress in multiphase flow—Is it an important parameter in CO2 corrosion of carbon steel pipelines?, Corrosion Science, 110 (2016) 35-45.

[29] W. Li, B.F.M. Pots, X. Zhong, S. Nesic, Inhibition of CO2 Corrosion of Mild Steel − Study of Mechanical Effects of Highly Turbulent Disturbed Flow, Corrosion Science, 126 (2017) 208-226.

[30] M. Abe, C. Takato, S. Hamada, M. Hayase, Cu Corrosion in Laminar Flow Using Microfluidic Channels, in: Proceedings of International Conference on Planarization/CMP Technology, Kobe, Japan, 2014, pp. 265-268.

Schlumberger-Private

[31] J. McGrady, J. Duff, N. Stevens, A. Cioncolini, M. Curioni, A. Banks, F. Scenini, Development of a Microfluidic Setup to Study the Corrosion Product Deposition in Accelerated Flow Regions, npj Materials Degradation, 1 (2017) 21.

[32] J. Sullivan, S. Mehraban, J. Elvins, In situ monitoring of the microstructural corrosion mechanisms of zinc–magnesium–aluminium alloys using time lapse microscopy, Corrosion Science, 53 (2011) 2208-2215.

[33] J. Światowska, P. Volovitch, K. Ogle, The anodic dissolution of Mg in NaCl and Na2SO4 electrolytes by atomic emission spectroelectrochemistry, Corrosion Science, 52 (2010) 2372-2378.

[34] P. Jiang, J.-L. Chen, F. Borondics, P.-A. Glans, M.W. West, C.-L. Chang, M. Salmeron, J. Guo, In situ soft X-ray absorption spectroscopy investigation of electrochemical corrosion of copper in aqueous NaHCO3 solution, Electrochemistry Communications, 12 (2010) 820-822.

[35] D. Burkle, R.D. Motte, W. Taleb, A. Kleppe, T. Comyn, S.M. Vargas, A. Neville, R. Barker, Development of an electrochemically integrated SR-GIXRD flow cell to study FeCO3 formation kinetics, Review of Scientific Instruments, 87 (2016) 105-125.

[36] D. Burkle, R. De Motte, W. Taleb, A. Kleppe, T. Comyn, S.M. Vargas, A. Neville, R. Barker, In situ SR-XRD study of FeCO3 precipitation kinetics onto carbon steel in CO2-containing environments: The influence of brine pH, Electrochimica Acta, 255 (2017) 127-144.

[37] T. Chen, A. Neville, K. Sorbie, Z. Zhong, In-situ monitoring the inhibiting effect of polyphosphinocarboxylic acid on CaCO3 scale formation by synchrotron X-ray diffraction, Chemical Engineering Science, 64 (2009) 912-918.

[38] J.E. Maslar, W.S. Hurst, W.J.B. Jr., J.H. Hendricks, In Situ Raman Spectroscopic Investigation of Stainless Steel Hydrothermal Corrosion, CORROSION, 58 (2002) 739-747.

[39] ASTM, Standard Practice for Laboratory Immersion Corrosion Testing of Metals, in: ASTM G31-72, ASTM International, West Conshohocken, Pennsylvania, 2004.

[40] Tenaris, Material Specification HS-80. http://www.tenaris.com/~/media/Files/ProductLiterature/OCTG/HS80_CoiledTubeDocs101909, 2014 (accessed 30 June 2017).

[41] E. Barmatov, T. Hughes, M. Nagl, Performance of Organic Corrosion Inhibitors on Carbon Steels and High Alloys in 4M Hydrochloric Acid, in: CORROSION, NACE International, Dallas, Texas, 2015.

[42] D. Taylor, T.A. Nieman, Effect of cell geometry on conductance measurements in flow cells, Analytica Chimica Acta, 159 (1984) 397-400.

[43] J.C. Myland, K.B. Oldham, Uncompensated Resistance. 1. The Effect of Cell Geometry, Analytical chemistry, 72 (2000) 3972-3980.

[44] D. Pike, N. Kapur, P. Millner, D. Stewart, Flow Cell Design for Effective Biosensing, Sensors, 13 (2012) 58-70.

[45] E. Nishikata, T. Ishii, T. Ohta, Viscosities of aqueous hydrochloric acid solutions, and densities and viscosities of aqueous hydroiodic acid solutions, Journal of Chemical & Engineering Data, 26 (1981) 254-256.

Schlumberger-Private

[46] M. Nordsveen, S. Nešić, R. Nyborg, A. Stangeland, A Mechanistic Model for Carbon Dioxide Corrosion of Mild Steel in the Presence of Protective Iron Carbonate Films—Part 1: Theory and Verification, CORROSION, 59 (2003) 443-456.

[47] R.L. Wabeke, Air contaminants and industrial hygiene ventilation: A handbook of practical calculations, problems, and solutions, CRC Press, 1998.

[48] A.V. Valdes, A. ; Marcano, S. ; Boggio, C., A Field Experience of Corrosion Inhibition During the Acid Fracturing of a Deep Oil Well Completed with 22 % Cr Duplex Steel in: Corrosion -National Associaton of Corrosion Engineers Anual Conference, 1993, pp. 1096-1103.

[49] E. Barmatov, T. Hughes, D. Eskin, Effect of surface roughness on corrosion behaviour of low carbon steel in inhibited 4 M hydrochloric acid under laminar and turbulent flow conditions, Corrosion Science, 103 (2015) 196-205.

[50] E. Barmatov, T.L. Hughes, Effect of corrosion products and turbulent flow on inhibition efficiency of propargyl alcohol on AISI 1018 mild carbon steel in 4M hydrochloric acid, Corrosion Science, 123 (2017) 170-181.

8. Figure Captions

Figure 1: Optical microscope image of the HS80^{TM} microstructure after chemical etching in 2% nital solution.

Figure 2: (a) Exploded view of the once-through flow cell used in this study; (b) cross-section through the flow cell indicating position of reference/counter electrode and HS80^{TM} carbon steel specimen in relation to the gasket. Note: the volume of the flow cell is 1 ml and the labels 1 to 7 are referred to in the body of the manuscript.

Figure 3: Geometry of gasket specified for the flow cell based on the iCell shape proposed by Pike et al. [44] – the central square indicates the size and position of the 1 cm^2 carbon steel specimen within the cell. The x and y scale bars show the gasket dimensions as displacements relative to the centre of the steel specimen.

Figure 4: (a) 3D constructed geometry of the flow cell within COMSOL Multiphysics and (b) axisymmetric model indicating the distributed mesh applied across the specimen to adequately resolve the concentration gradient in the boundary layer. Note: a fine mesh was applied to the edges of the steel specimen where sharp changes in specie concentration were anticipated.

Schlumberger-Private

Figure 5: Computational results from COMSOL Multiphysics indicating the velocity fields within the flow cell at a distance of 1 mm perpendicularly outwards from the steel surface and the velocity profiles across the leading edge, trailing edge and centre line of the specimen at a distance of 1 mm outwards from the steel surface. The results correspond to three different flow rates of (a) 1, (b) 10, and (c) 25 ml min^{-1} through the flow cell.

Figure 6: Concentration maps generated within COMSOL Multiphysics across the base of the flow cell where the steel specimen is positioned. The simulation performed is for an inlet flow rate of 1 ml min^{-1}, continuous HCl concentration of 4 mol L^{-1} and defined uninhibited corrosion current density of 86.2 mA cm^{-2}. The maps presented relate to (a) H^+ and (b) Fe^{2+} ion concentrations.

Figure 7: Schematic of the complete acidizing flow cell experimental setup used in this study. 4 mol L^{-1} NaCl solution is delivered at a flow rate of 10 ml min^{-1} from the 10 L container into the vessel containing 1 L of 4 mol L^{-1} HCl and 0.05 wt.% PA. At the same time, the solution from the 1 L vessel is transferred out through the flow cell and into a waste container at an identical flow rate.

Figure 8: Tafel polarisation plots for HS80™ steel specimens after exposure to inhibited HCl – NaCl solutions for 3h under static conditions in a 1 L closed vessel. Acid concentration was achieved by dilution of 4 mol L^{-1} HCl (containing 0.05 wt.% PA) with 4 mol L^{-1} uninhibited NaCl solution. Solution HCl concentrations were 4, 0.04 and 4×10^{-4} mol L^{-1}. Separate specimens were used to construct the anodic and cathodic Tafel slopes and were obtained by polarising from OCP to either +100 or -200 mV at a scan rate of 0.5 mV s^{-1}.

Figure 9: Corrosion rates obtained for HS80TM steel specimens in HCl – NaCl inhibited solutions from either 12 LPR measurements averaged over 3h (expressed in mA cm-2 and shown on the primary y axis) or 3h mass-loss tests (expressed in g m-2 h-1 and shown on the secondary y axis). Tests were performed in static conditions in a closed 1 L vessel over HCl concentrations ranging from 4 mol L-1 down to 0.0004 mol L-1. Acid concentration was achieved by dilution of 4 mol L-1 HCl (containing 0.05 wt.% PA) with 4 mol L-1 uninhibited NaCl solution. The scatter bands for the LPR data (shown by the wider caps) represent the highest and lowest corrosion rates determined across all individual LPR measurements over all 3h experiments at each condition. The scatter bands for the mass-loss data (shown by the smaller caps) represent the maximum and minimum recorded corrosion rates across all 3h mass-loss tests in each environment. Note: through the application of Faraday's Law, 1 mA cm-2 as a corrosion current density is equivalent to approximately 10.4 g m-2 h-1.

Schlumberger-Private

Figure 10: Comparison of (a) OCP (vs 4 mol L^{-1} Ag/AgCl) and (b) reciprocal of charge-transfer resistance determined from static 3h experiments in a closed 1 L vessel with those obtained throughout the flow cell dilution process. Individual points represent the average values from 3h static experiments at times where the solution chemistries match those observed within the flow cell. Scatter bands relate to the maximum and minimum values observed across all repeat experiments. Both dilution line graphs correspond to the LPR measurements performed every 5 minutes throughout the duration of the flow cell experiment whereby 4 mol L^{-1} HCl (containing 0.05 wt.% PA) was diluted with 4 mol L^{-1} uninhibited NaCl solution and pumped through the flow cell at a rate of 10 ml min^{-1}. The HCl concentration of the HCl – NaCl mixture travelling through the cell is indicated by the dotted linear plot in both graphs and relates to the secondary y-axis.

Figure 11: Comparison of the corrosion rates determined from static 3h experiments in a closed 1 L vessel with those obtained throughout the flow cell dilution process (all expressed in mA cm^{-2} for ease of comparison). The two sets of individual points represent the average values from 3h static experiments at times where the solution chemistries match those observed within the flow cell and were obtained from either mass-loss or averaged LPR measurements over 3h. The scatter bands for the LPR data (shown by the wider caps) represent the highest and lowest corrosion rates determined across all individual LPR measurements over all 3h experiments at each condition. The scatter bands for the mass-loss data (shown by the smaller caps) represent the maximum and minimum recorded corrosion rates across all 3h mass-loss tests in each environment. Both dilution line graphs correspond to the LPR measurements performed every 5 minutes throughout the duration of the flow cell experiment whereby 4 mol L^{-1} HCl (containing 0.05 wt.% PA) was diluted with 4 mol L^{-1} uninhibited NaCl solution and pumped through the flow cell at a rate of 10 ml min^{-1}. The HCl concentration of the HCl – NaCl mixture travelling through the cell is indicated by the dotted linear plot in both graphs and relates to the secondary y-axis. Note: through the application of Faraday's Law, 1 mA cm^{-2} as a corrosion current density is equivalent to approximately 10.4 g m^{-2} h^{-1}.

Schlumberger-Private

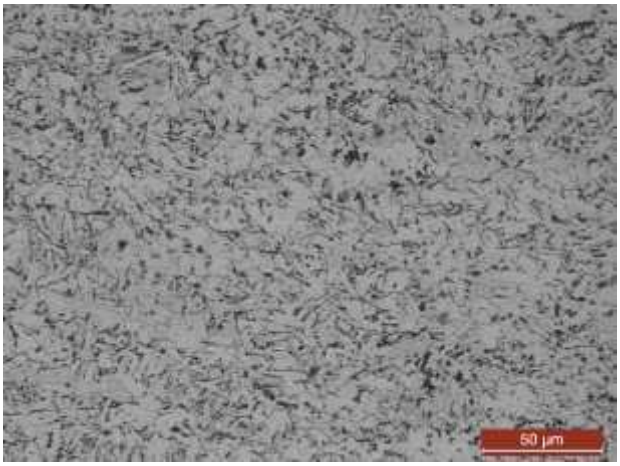

Figure 1: Optical microscope image of the HS80™ microstructure after chemical etching in 2% nital solution.

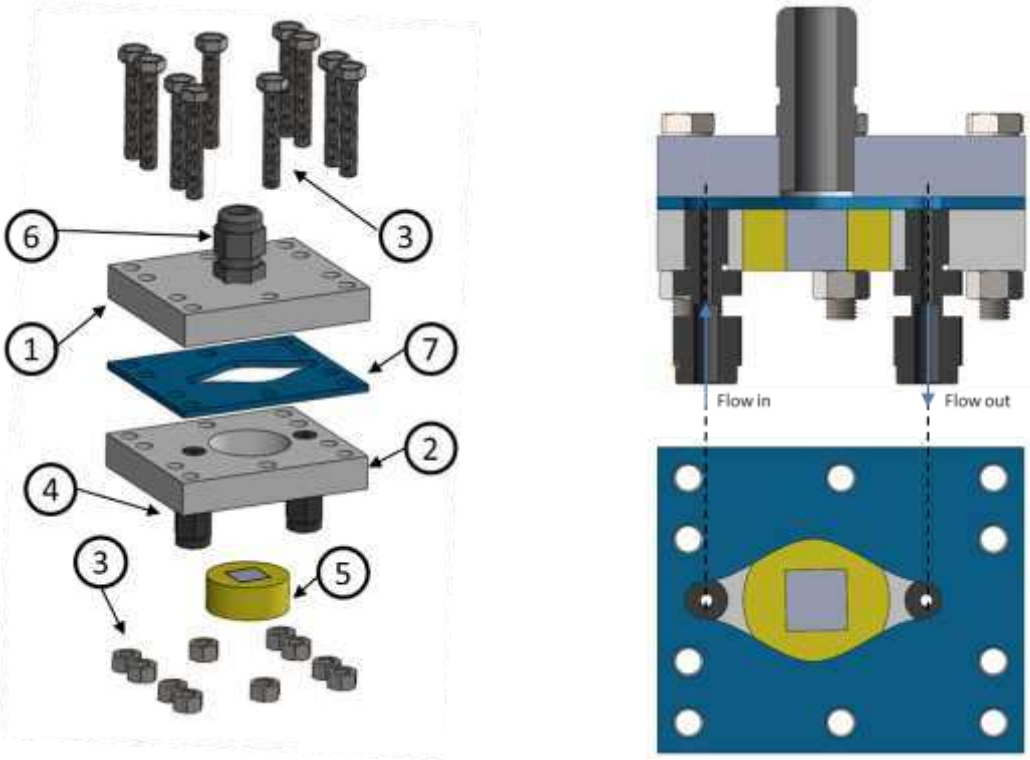

(a) **(b)**

Figure 2: (a) Exploded view of the once-through flow cell used in this study; (b) cross-section through the flow cell indicating position of reference/counter electrode and HS80™ carbon steel specimen in relation to the gasket. Note: the volume of the flow cell is 1 ml and the labels 1 to 7 are referred to in the body of the manuscript.

Schlumberger-Private

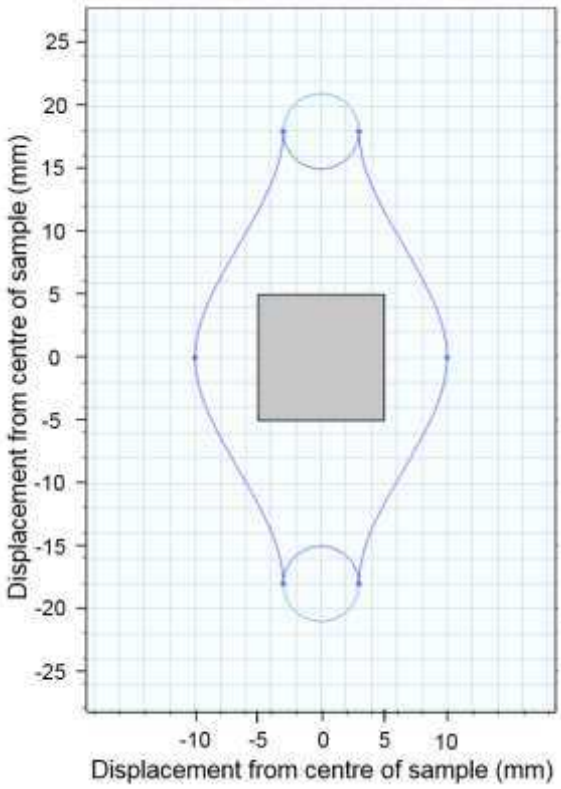

Figure 3: Geometry of gasket specified for the flow cell based on the iCell shape proposed by Pike et al. [44] – the central square indicates the size and position of the 1 cm^2 carbon steel specimen within the cell. The x and y scale bars show the gasket dimensions as displacements relative to the centre of the steel specimen.

Schlumberger-Private

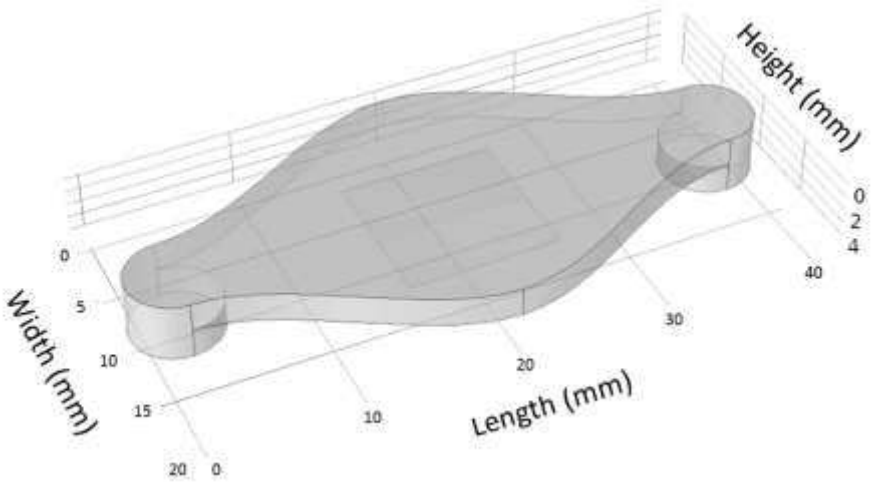

(a)

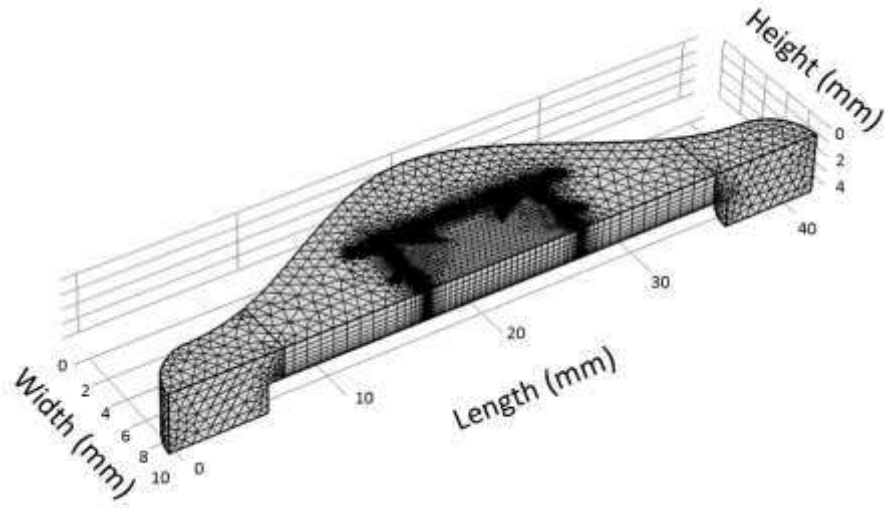

(b)

Figure 4: (a) 3D constructed geometry of the flow cell within COMSOL Multiphysics and (b) axisymmetric model indicating the distributed mesh applied across the specimen to adequately resolve the concentration gradient in the boundary layer. Note: a fine mesh was applied to the edges of the steel specimen where sharp changes in specie concentration were anticipated.

Schlumberger-Private

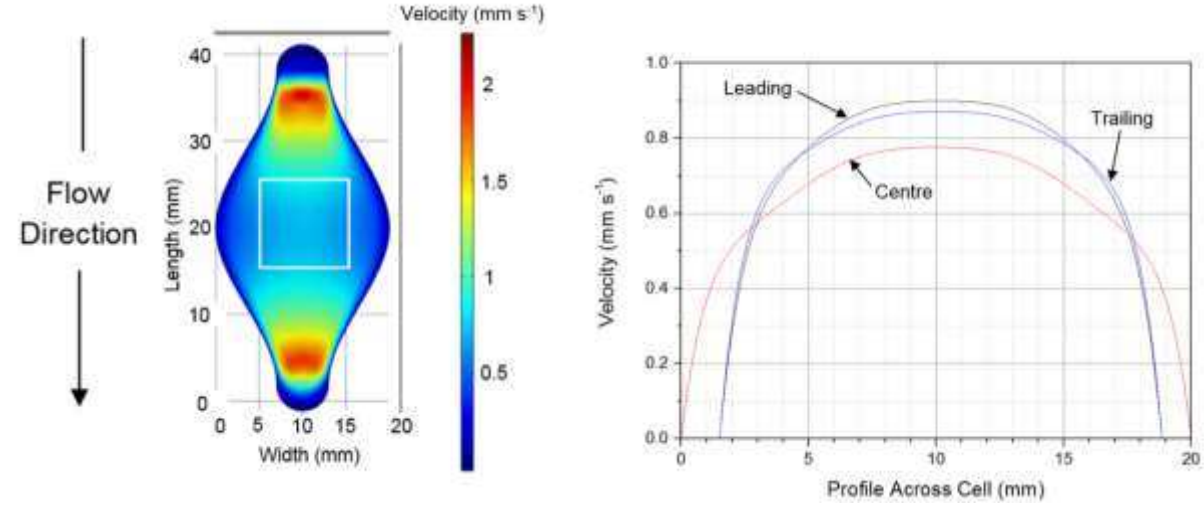

(a)

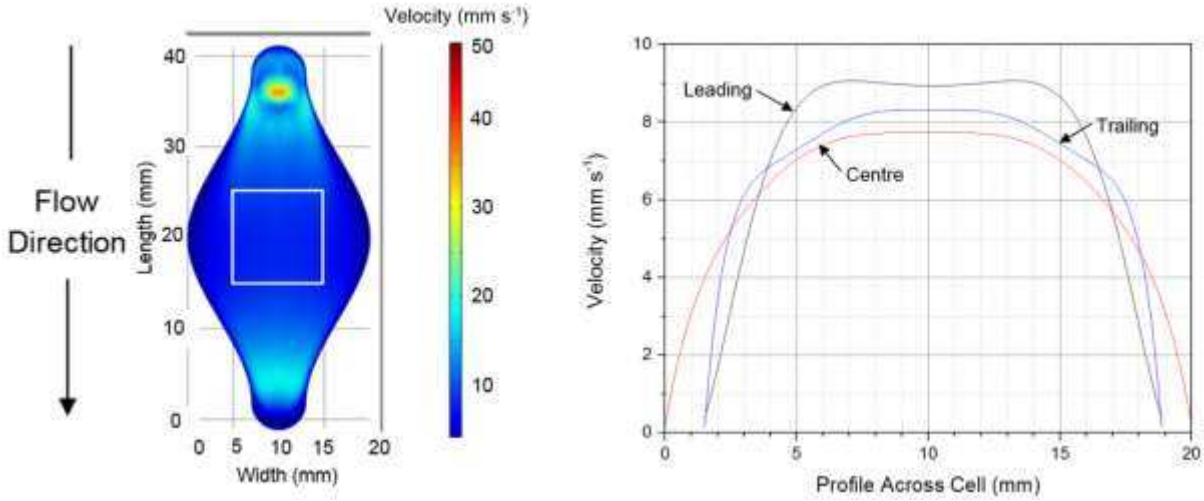

(b)

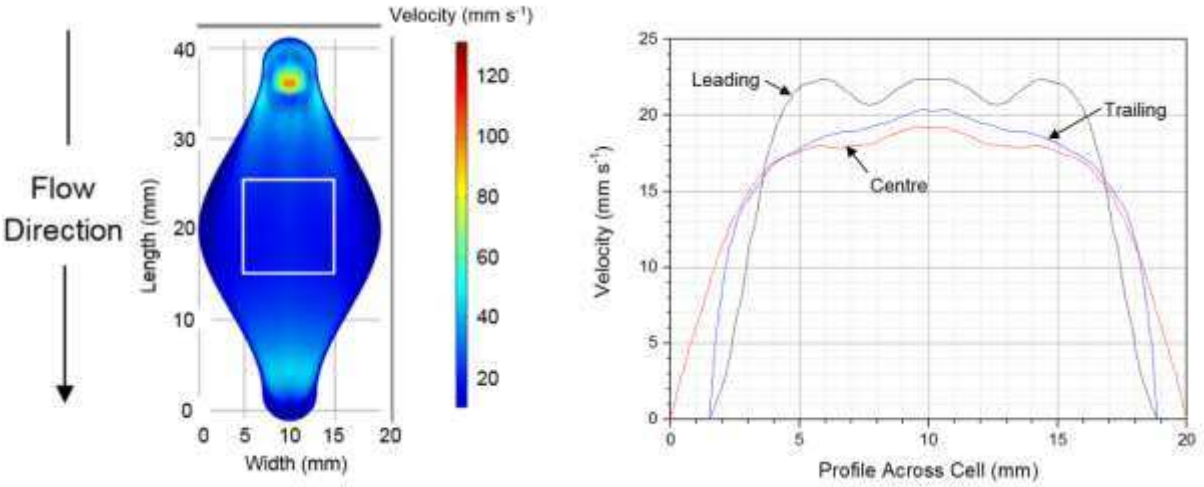

(c)

Figure 5: Computational results from COMSOL Multiphysics indicating the velocity fields within the flow cell at a distance of 1 mm perpendicularly

Schlumberger-Private

outwards from the steel surface and the velocity profiles across the leading edge, trailing edge and centre line of the specimen at a distance of 1 mm outwards from the steel surface. The results correspond to three different flow rates of (a) 1, (b) 10, and (c) 25 ml min^{-1} through the flow cell.

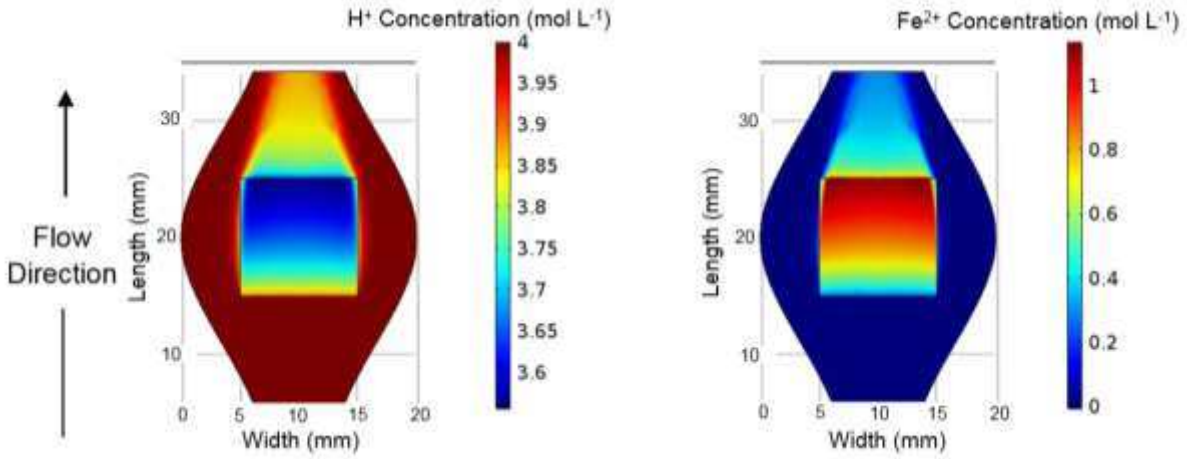

(a) **(b)**

Figure 6: Concentration maps generated within COMSOL Multiphysics across the base of the flow cell where the steel specimen is positioned. The simulation performed is for an inlet flow rate of 1 ml min^{-1}, continuous HCl concentration of 4 mol L^{-1} and defined uninhibited corrosion current density of 86.2 mA cm^{-2}. The maps presented relate to (a) H^+ and (b) Fe^{2+} ion concentrations.

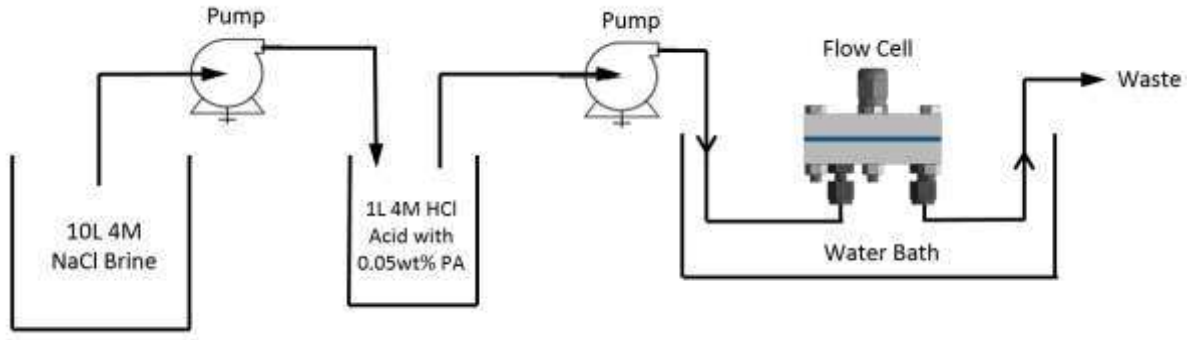

Figure 7: Schematic of the complete acidizing flow cell experimental setup used in this study. 4 mol L^{-1} NaCl solution is delivered at a flow rate of 10 ml min^{-1} from the 10 L container into the vessel containing 1 L of 4 mol L^{-1} HCl and 0.05 wt.% PA. At the same time, the solution from the 1 L vessel is transferred out through the flow cell and into a waste container at an identical flow rate.

Schlumberger-Private

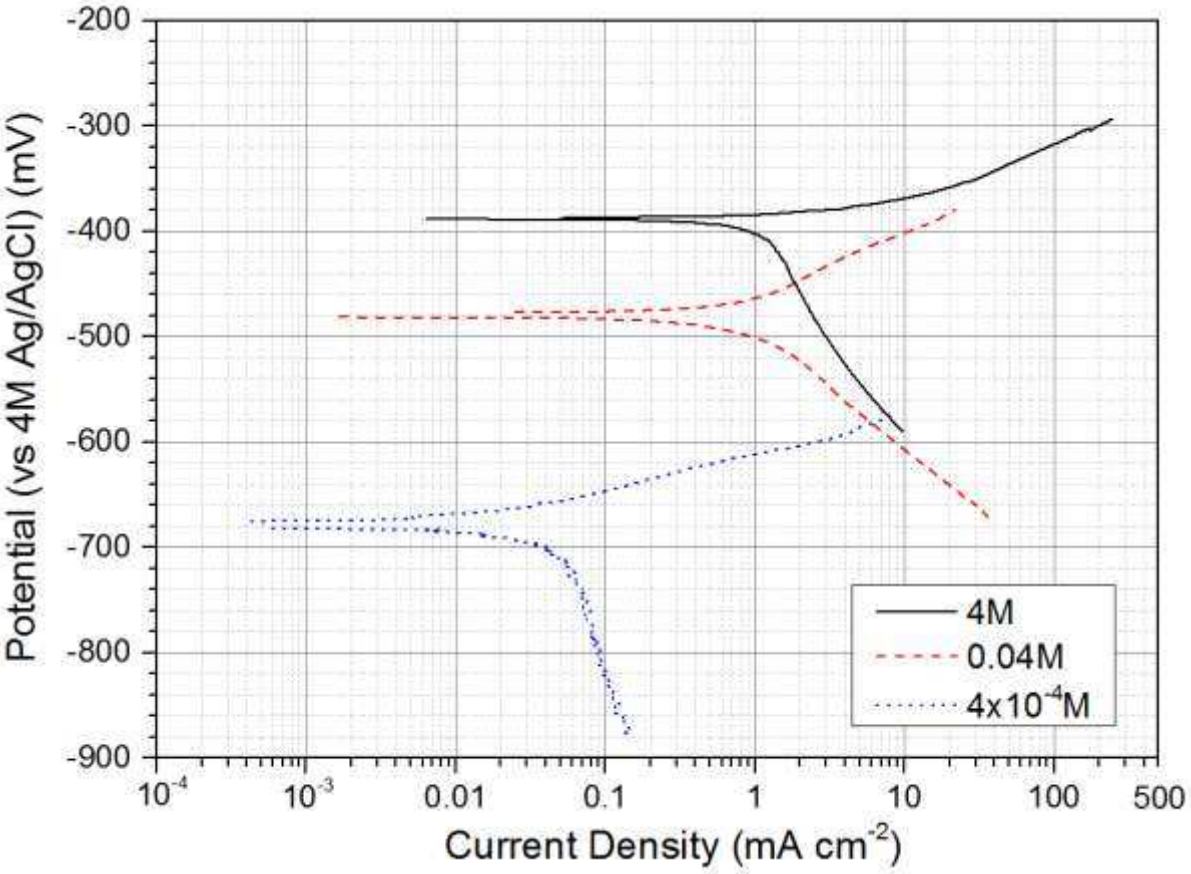

Figure 8: Tafel polarisation plots for HS80™ steel specimens after exposure to inhibited HCl – NaCl solutions for 3h under static conditions in a 1 L closed vessel. Acid concentration was achieved by dilution of 4 mol L^{-1} HCl (containing 0.05 wt.% PA) with 4 mol L^{-1} uninhibited NaCl solution. Solution HCl concentrations were 4, 0.04 and 4×10^{-4} mol L^{-1}. Separate specimens were used to construct the anodic and cathodic Tafel slopes and were obtained by polarising from OCP to either +100 or -200 mV at a scan rate of 0.5 mV s^{-1}.

Schlumberger-Private

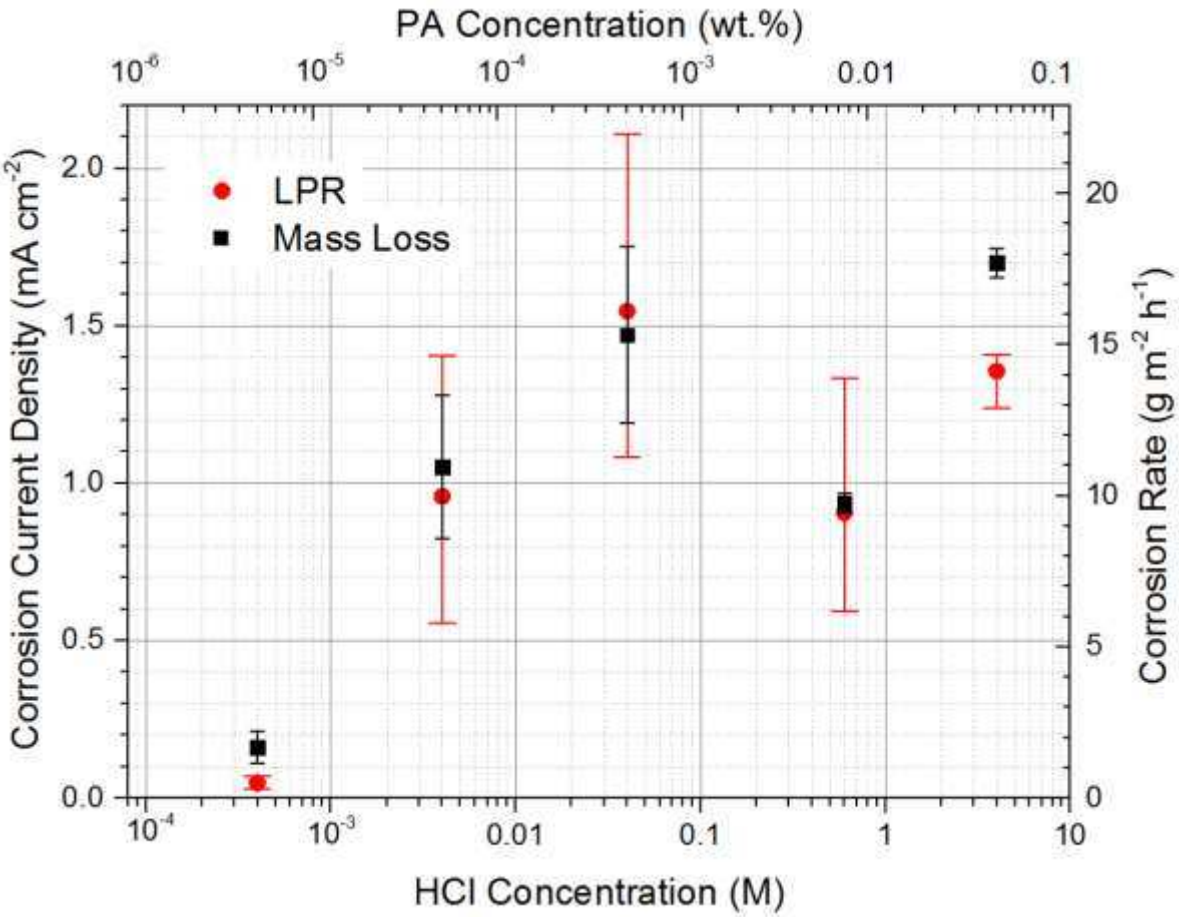

Figure 9: Corrosion rates obtained for HS80™ steel specimens in HCl – NaCl inhibited solutions from either 12 LPR measurements averaged over 3h (expressed in mA cm^{-2} and shown on the primary y axis) or 3h mass-loss tests (expressed in g m^{-2} h^{-1} and shown on the secondary y axis). Tests were performed in static conditions in a closed 1 L vessel over HCl concentrations ranging from 4 mol L^{-1} down to 0.0004 mol L^{-1}. Acid concentration was achieved by dilution of 4 mol L^{-1} HCl (containing 0.05 wt.% PA) with 4 mol L^{-1} uninhibited NaCl solution. The scatter bands for the LPR data (shown by the wider caps) represent the highest and lowest corrosion rates determined across all individual LPR measurements over all 3h experiments at each condition. The scatter bands for the mass-loss data (shown by the smaller caps) represent the maximum and minimum recorded corrosion rates across all 3h mass-loss tests in each environment. Note: through the application of Faraday's Law, 1 mA cm^{-2} as a corrosion current density is equivalent to approximately 10.4 g m^{-2} h^{-1}.

Schlumberger-Private

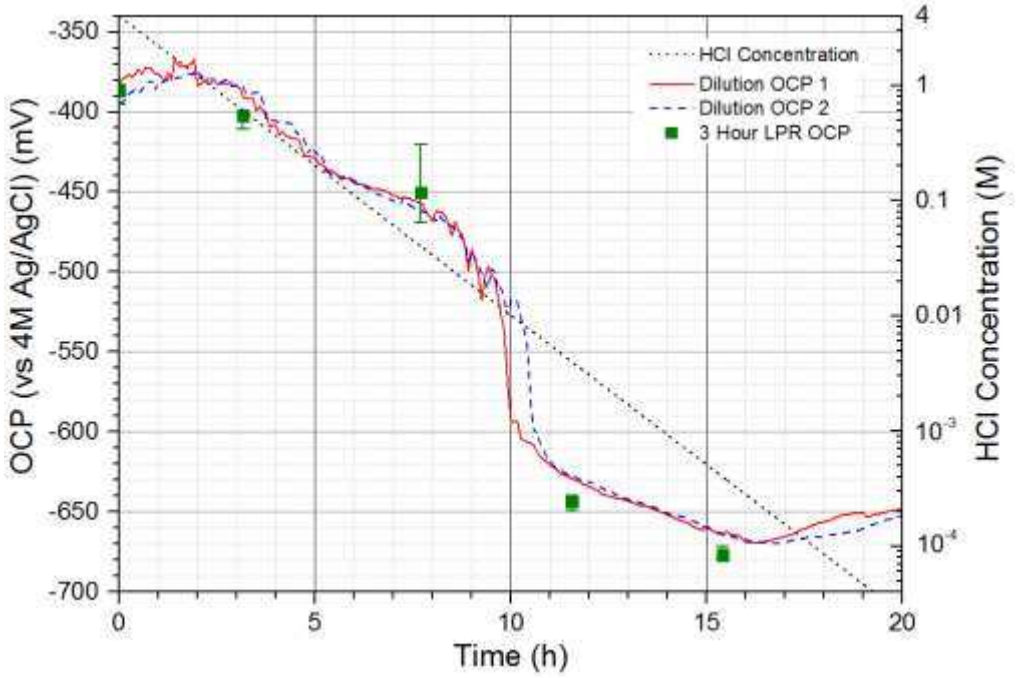

(a)

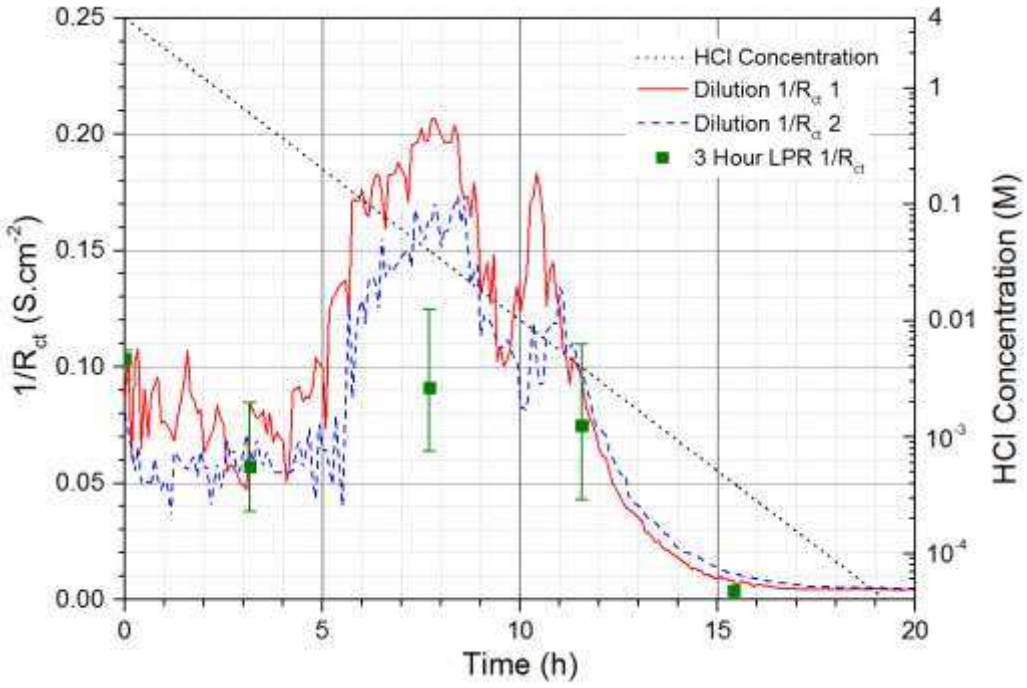

(b)

Figure 10: Comparison of (a) OCP (vs 4 mol L^{-1} Ag/AgCl) and (b) reciprocal of charge-transfer resistance determined from static 3h experiments in a closed 1 L vessel with those obtained throughout the flow cell dilution process. Individual points represent the average values from 3h static experiments at times where the solution chemistries match those observed within the flow cell. Scatter bands relate to the maximum and minimum values observed across all repeat experiments. Both dilution line graphs correspond to the LPR

Schlumberger-Private

measurements performed every 5 minutes throughout the duration of the flow cell experiment whereby 4 mol L^{-1} HCl (containing 0.05 wt.% PA) was diluted with 4 mol L^{-1} uninhibited NaCl solution and pumped through the flow cell at a rate of 10 ml min^{-1}. The HCl concentration of the HCl – NaCl mixture travelling through the cell is indicated by the dotted linear plot in both graphs and relates to the secondary y-axis.

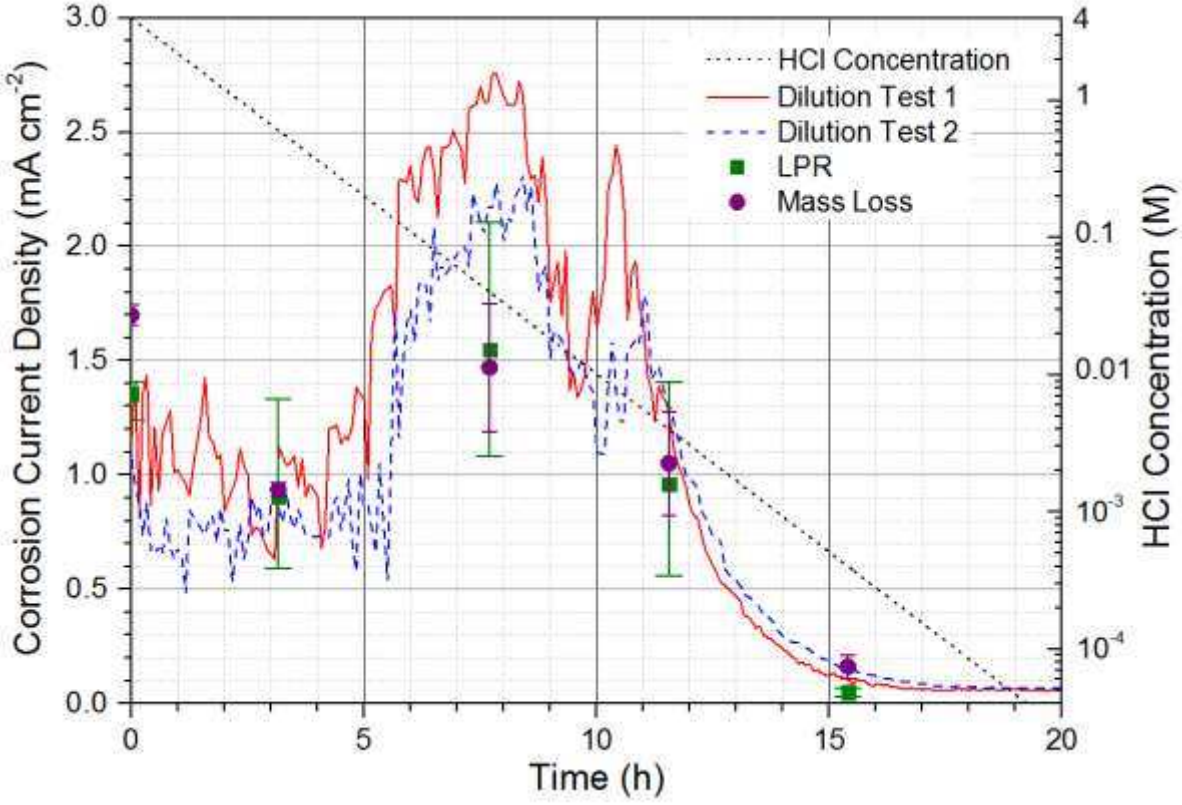

Figure 11: Comparison of the corrosion rates determined from static 3h experiments in a closed 1 L vessel with those obtained throughout the flow cell dilution process (all expressed in mA cm^{-2} for ease of comparison). The two sets of individual points represent the average values from 3h static experiments at times where the solution chemistries match those observed within the flow cell and were obtained from either mass-loss or averaged LPR measurements over 3h. The scatter bands for the LPR data (shown by the wider caps) represent the highest and lowest corrosion rates determined across all individual LPR measurements over all 3h experiments at each condition. The scatter bands for the mass-loss data (shown by the smaller caps) represent the maximum and minimum recorded corrosion rates across all 3h mass-loss tests in each environment. Both dilution line graphs correspond to the LPR measurements performed every 5 minutes throughout the duration of the flow cell experiment whereby 4 mol L^{-1} HCl (containing 0.05 wt.% PA) was diluted with 4 mol L^{-1} uninhibited NaCl solution and pumped through the flow cell at a rate of 10 ml min^{-1}. The HCl concentration of the HCl

Schlumberger-Private

– NaCl mixture travelling through the cell is indicated by the dotted linear plot in both graphs and relates to the secondary y-axis. Note: through the application of Faraday's Law, 1 mA cm^{-2} as a corrosion current density is equivalent to approximately 10.4 g m^{-2} h^{-1}.

Schlumberger-Private